

Declaration of Academic Integrity

Final Year Project

Student's (official) name: Hakyung Yi

Professor's name: Phee Soo Jay Louis

School: Mechanical and Aerospace Engineering (MAE)

Assignment Title: HOME POSITION TUNING FOR ENDOSCOPIC SURGICAL ROBOTS

Declaration

I/We* have read and understood the guidelines on academic dishonesty as found at <https://bit.ly/3pDQgbw> and the penalties for academic dishonesty (as stated in 'General Instructions'), and declare that this assignment is my/our own work and does not involve plagiarism or collusion according to the University's honour code and pledge. I/We have acknowledged and appropriately referenced the sources used in my/our work, as well as the use of Artificial Intelligence (AI) sources. I/We have attached the 'Description of AI Sources' form to my/our assignment to describe the use of AI sources in my/our work. I/We have also not submitted any part of this assignment for another course.

Student's signature:

HAKYUNG YI



Date: 12 Nov. 24

Description of AI Sources

Instructions:

1. You do not need to submit this form if you have not used any AI sources in your work.
2. If you have used AI sources in your assignment, please acknowledge and reference them in your work (refer to the guidelines on NTULearn main course site for more details).
3. Please provide information on the AI sources used and how you have used these sources in your work by completing the table below.
4. Please be aware that the AI sources used should complement your own critical thinking and judgment.
5. When submitting your assignment in hard copy, attach both the 'Declaration of Academic Integrity' and 'Description of AI sources' forms to your assignment before submission.
6. If you are submitting your assignment in soft copy, deposit this form into a separate folder that your tutor can create for you on your NTULearn tutorial group course site.
7. Do not submit this form to Turnitin.

Student's name: Hakyung Yi

Submission Date: 12 Nov. 24

I/We* have used AI sources in my/our work. Here are the descriptions of how the AI sources have been used:

AI Sources used (name of AI tool and URL)	Prompts used	How AI sources are used (e.g., To organize research materials, answer questions on a particular topic, and check grammar and spelling)
ChatGPT (OpenAI)	Rewrite sentences using formal and academic vocabulary	To use more appropriate and academic vocabulary suitable for research paper.
ChatGPT (OpenAI)	Check for grammar or spelling mistakes	To prevent from making grammar errors or spelling mistakes.

Acad Year

2024

PROJECT NO.

B217

HOME POSITION TUNING FOR ENDOSCOPIC SURGICAL ROBOTS

HOME POSITION TUNING FOR ENDOSCOPIC SURGICAL ROBOTS



HAKYUNG YI

**SCHOOL OF MECHANICAL AND AEROSPACE ENGINEERING
NANYANG TECHNOLOGICAL UNIVERSITY**

Year 2024

HOME POSITION TUNING FOR ENDOSCOPIC SURGICAL ROBOTS

SUBMITTED

BY

HAKYUNG YI

SCHOOL OF MECHANICAL AND AEROSPACE ENGINEERING

A final-year project report

presented to

Nanyang Technological University

in partial fulfillment of the

requirements for the

Degree of Bachelor of Engineering (Mechanical Engineering)

Nanyang Technological University

Year 2024

ABSTRACT

This project presents a control algorithm for home position tuning in endoscopic surgical robots using the tendon-sheath mechanism with sensorless control at the distal end. The algorithm takes real-time motor current feedback to calibrate the home position, a method well-suited for minimally invasive surgery due to its compact design. The approach uses an MX106 Dynamixel motor and tendon-sheath mechanism integrated into a testbed with adjustable components to simulate varying surgical conditions. The algorithm's method involves detecting peak motor currents, which correspond to the sheath's extreme positions, allowing for an accurate home position computation. The algorithm's precision and adaptability are measured by conducting trials with various sheath curvatures and contact angles. Results indicate that the algorithm has a considerably high accuracy in detecting the home position, suggesting its strong potential in enhancing the precision of endoscopic surgical robots. Future work will include refining the algorithm to handle additional sheath variations and to adapt in diverse surgical environments.

ACKNOWLEDGEMENT

Foremost, I would like to express my sincere gratitude to Professor Phee Soo Jay Louis for providing me with the opportunity to contribute to the project. His guidance, expertise, and insightful feedback during presentations ensured that the project progressed in the right direction.

I extend my deep appreciation to the research fellows in Prof. Phee's team, including Dr. Lai Wenjie and Dr. Liu Jiajun. Their unwavering support and invaluable advice have been essential for a comprehensive understanding of the project. Without their guidance and help, this project would not have been possible.

Lastly, I thank the Robotics Research Center (RRC) and Campus for Research Excellence and Technological Enterprise (CREATE) for their generous provision and permission to use their facilities.

TABLE OF CONTENTS

ABSTRACT.....	5
ACKNOWLEDGEMENT.....	6
TABLE OF FIGURES.....	9
LIST OF TABLES	11
1. INTRODUCTION.....	12
1.1 BACKGROUND.....	12
1.2 OBJECTIVES	14
1.3 SCOPE	14
2. LITERATURE REVIEW	15
2.1 ROBOT-ASSISTED SURGERY.....	15
2.1.1 <i>Da Vinci Surgical System</i>	15
2.1.2 <i>EndoMaster</i>	17
2.2 TENDON SHEATH MECHANISM	19
2.2.1 <i>Mechanism of TSM</i>	19
2.2.2 <i>Control Challenges in TSM-Driven Mechanism</i>	21
2.2.3 <i>Haptic Feedback</i>	22
2.2.4 <i>Home Positioning</i>	24
2.3 ROBOTIC GRIPPERS	25
2.3.1 <i>Design and Kinematics of Robotic Grippers</i>	25
2.3.1 <i>Force Transmission in TSM-Driven Grippers</i>	26
2.3.2 <i>Robotic Gripper Control</i>	27
3. METHODOLOGY	29
3.1 SYSTEM OVERVIEW	29
3.2 HOME POSITION TUNING APPROACH	29
3.3 EXPERIMENTAL SETUP	31
3.4 DATA COLLECTION AND ANALYSIS	36
4. IMPLEMENTATION	37
4.1 HARDWARE IMPLEMENTATION	37
4.1.1 <i>MX106 Dynamixel Motor</i>	37

4.1.2	<i>Distal Pulley & Bearing</i>	40
4.1.3	<i>Slidable Wall</i>	41
4.2	SOFTWARE IMPLEMENTATION.....	44
4.2.1	<i>Two's Complement</i>	45
4.2.2	<i>Moving Average Filter</i>	47
4.2.3	<i>Peak Detection Algorithm</i>	48
4.2.4	<i>Mapping of Motor Current to Torque</i>	51
4.2.5	<i>Home Positioning Control Algorithm Development</i>	52
5.	RESULTS AND DISCUSSION	56
5.1	RESULTS	56
5.1.1	<i>Straight Configuration</i>	57
5.1.2	<i>Curved Configuration, Sin(0.5x),</i>	60
5.1.3	<i>Curved Configuration, Sin(x)</i>	63
5.2	DISCUSSION	66
5.2.1	<i>Performance of the Control Algorithm</i>	66
5.2.4	<i>Advantages of Using Motor Current Readings</i>	70
5.2.5	<i>Limitations</i>	70
6.	FUTURE WORKS.....	72
7.	CONCLUSION	74
8.	REFERENCES.....	75

TABLE OF FIGURES

Figure 1. 1 Tendon sheath mechanism (TSM).....	13
Figure 2. 1 Da Vinci surgical system (The image "2023-09 - Robot chirurgien Da Vinci Xi - Centre hospitalier de Vesoul - 16" by A.BourgeoisP is licensed under the Creative Commons Attribution License) [8]	15
Figure 2. 2 View of the setup of the patient and the da Vinci surgical robot (Images from open-access journals licensed under the Creative Commons Attribution License) [14]	16
Figure 2. 3 Colonic endoscopic submucosal dissection performed using the latest version of the EndoMaster EASE System (Images are reused from open-access journals licensed under the Creative Commons Attribution License) [18]	18
Figure 2. 4 "Capstan equation diagram" by Krishnavedala is licensed under the Creative Commons Attribution License	19
Figure 3. 1 Home Position Tuning Steps	30
Figure 3. 2 Gripper Inside Endoscope Channel	31
Figure 3. 3 (a) CAD Experiment Setup (b) Actual Experiment Setup	32
Figure 3. 4 Straight Configuration	33
Figure 3. 5 Curved Configuration, $\sin(0.5x)$	33
Figure 3. 6 Curved Configuration $\sin(x)$	34
Figure 3. 7 Data Collection and Analysis Flowchart	36
Figure 4. 1 MX106 Dynamixel motors [61]	37
Figure 4. 2 MX106 Dynamixel performance chart.....	38
Figure 4. 3 (a) Distal Pulley with a pointed tip & Bearings (b) Cross-sectional view of distal pulley and bearings	40
Figure 4. 4 Prototype No. 1 with attached wall	41
Figure 4. 5 Prototype No. 2 with detachable wall equipped with step holes	42
Figure 4. 6 (a) CAD model of the prototype's base (b) Real setup of the prototype on a mounting board	43
Figure 4. 7 (a) Sheath-holder type A (b) Sheath-holder type B (c) Sheath-holder type A near distal pulley (d) Sheath-holders near motors	44

Figure 4. 8 Code Flow	42
Figure 4. 9 Motor's current feedback before implementing the number conversion algorithm. Hence, the readings are highly erratic.....	45
Figure 4. 10 Two's Conversion Flowchart.....	46
Figure 4. 11. Current feedback after applying moving average filter of various window sizes: 5, 10, 20, 30.....	47
Figure 4. 12 Current feedback after applying the moving average filter of size 8	48
Figure 4. 13 Peak detection algorithm flowchart.....	49
Figure 4. 14 Home position calculation procedures flowchart	52
Figure 4. 15 (a) Initial Position (b) First peak angle – touches the right wall (b) second peak angle –touches the left wall.....	53
Figure 4. 16 3D-printed distal pulley touching the right and left wall	54
Figure 5. 1 Straight, Smallest Angle – 52.7° Graph [Current vs Time]	57
Figure 5. 2 Straight, Middle Angle – 53.3° Graph [Current vs Time].....	58
Figure 5. 3 Straight, Largest Angle – 53.9° Graph [Current vs Time]	59
Figure 5. 4 Sin(0.5x), Smallest Angle, 52.7° [Current vs Time]	60
Figure 5. 5 Sin(0.5x), Middle Angle, 53.3° [Current vs Time].....	61
Figure 5. 6 Sin(0.5x), Largest Angle, 53.9° [Current vs Time]	62
Figure 5. 7 Sin(x), Smallest Angle, 52.7° [Current vs Time]	63
Figure 5. 8 Sin(x), Middle Angle, 53.3° [Current vs Time].....	64
Figure 5. 9 Sin(x), Largest Angle, 53.9° [Current vs Time]	65
Figure 5. 10 Graph of Error, Configuration, and Contact Angle	66
Figure 5. 11 Graph of Average Error vs Configuration.....	67
Figure 5. 12 Graph of Average Error vs Contact Angle	68

LIST OF TABLES

Table 1: Compiled Data of θ_{err}	56
Table 2: Average Error Computed in Straight, Smallest Angle – 52.7°	57
Table 3 Average Error Computed in Straight, Middle Angle – 53.3°	58
Table 4 Average Error Computed in Straight, Largest Angle – 53.9°	59
Table 5 Average Error Computed in $\sin(0.5x)$, Smallest Angle – 52.7°	60
Table 6 Average Error Computed in $\sin(0.5x)$, Middle Angle – 53.3°	61
Table 7 Average Error Computed in $\sin(0.5x)$, Largest Angle – 53.9°	62
Table 8 Average Error Computed in $\sin(x)$, Smallest Angle – 52.7°	63
Table 9 Average Error Computed in $\sin(x)$, Middle Angle – 53.3°	64
Table 10 Average Error Computed in $\sin(x)$, Largest Angle – 53.9°	65

1. INTRODUCTION

1.1 Background

Surgical robots transformed the field of minimally invasive surgery. Minimally invasive robotic surgeries bring benefits to surgeons in terms of teleoperation capability, improved dexterity, enhanced stereoscopic vision, tremor reduction, and reduced fatigue. It also provides patients with faster recovery, lower postoperative infection rates, and better cosmetic results [1]. They are gradually replacing open surgeries as they are gaining more popularity [2]. According to the Healthcare Robotics Market report published by Value Market Research, its market is predicted to reach \$14,095 billion in 2026 [3, 4].

The most popular minimally invasive surgical approaches are laparoscopic surgery and flexible robotic endoscopy. Laparoscopy includes making small holes, also known as keyholes, where a camera and special tools are inserted to operate. This lessens the consequences of regular open surgery – pain, hospital stay, and recovery time [5, 6]. Robotic laparoscopy like da Vinci is also commonly used in departments such as urology, gynecology, and general surgery. Their setup commonly includes a control station for the surgeon, a sharp 3D vision system, and a patient-side cart with robotic arms.

In contrast, endoscopic surgery uses an endoscope, a flexible tube equipped with a light source and camera, to access interior organs through tiny incisions or natural orifices. It enables the diagnosis and treatment of gastrointestinal disorders without leaving any abdominal incision [7]. It can approach desired targets such as tissues or gastrointestinal tracts using flexible robotic arms to perform surgical tasks.

Central to the functionality of these flexible robotic arms is the tendon-sheath mechanism (TSM) [7]. This mechanism mirrors the structure of flexible human tendons, where cables are housed within hollow wires, like those in ligaments. This facilitates precise and

controlled movement of the robotic arms, mimicking the flexibility and functionality of human anatomy.



Figure 1. 1 Tendon sheath mechanism (TSM)

Moreover, TSM is used to control the movement of robotic grippers, a component responsible for grasping tissues or carrying out surgical tasks such as suturing [8-9]. The tendons within the tendon-sheath mechanism are connected to actuators and motors, which control their contraction and extension. As the tendons move within their sheaths, they transmit forces to the robotic gripper, causing it to open and close.

A key to the effectiveness of the TSM in flexible endoscopic surgical robots is the precise initial positioning of the robotic gripper. The gripper must be initialized to its home position upon installation, ensuring that all joints are accurately positioned at their predefined neutral states. This initialization process is crucial as it forms the basis for subsequent surgical maneuvers, influencing the accuracy and safety of procedures. Currently, however, the initialization process relies heavily on manual adjustments, which can lead to human error and inconsistent results [10]. This is particularly problematic in TSM, where friction and accumulated angles complicate the control of the distal instruments' positions.

1.2 Objectives

A promising solution to the issue of manual adjustments is using the motor current readings to tune the homing position of the surgical instruments. Motor current data can provide valuable insights into the torque and resistance, allowing for real-time adjustments of the robotic gripper to ensure accurate positioning [11].

Given that there is a lack of control algorithms for integrating these sensor readings into instruments' starting positions, this project focuses on proposing innovative solutions that automate the calibration process. The primary objective of this project is to develop such an algorithm, which would improve the efficiency, reliability, and safety of robotic endoscopic procedures.

1.3 Scope

This project focuses on developing a control algorithm that calibrates home position based on motor's current readings. The current algorithm supports a single degree of freedom (1-DOF), which is yet insufficient to be applied in advanced surgical robots that require complex multi-DOF systems. To measure the algorithm's performance, it is tested in a simulated environment with a 1-meter flexible tendon-sheath segment of various curvatures and contact angles. The prototype setup is designed to demonstrate the feasibility of the control algorithm, and hence there remains a gap between this laboratory model and an actual surgical environment. The project relies on basic laboratory equipment, where for the end effector, a pulley with a pointed tip is used instead of a robotic gripper. Despite these constraints, the algorithm's performance will be assessed through controlled experiments to explore its applicability in real-world surgeries .

2. LITERATURE REVIEW

2.1 Robot-Assisted Surgery

2.1.1 Da Vinci Surgical System

Da Vinci Surgical System, developed by Intuitive Surgical, is a robotic surgical system that uses a minimally invasive surgical approach [12]. It consists of three major components: a surgeon's console, a patient-side cart with robotic arms, and a high-definition 3D vision system [13].



Figure 2. 1 Da Vinci surgical system (The image "2023-09 - Robot chirurgien Da Vinci Xi - Centre hospitalier de Vesoul - 16" by A.BourgeoisP is licensed under the Creative Commons Attribution License) [8]

A surgeon console is where a surgeon can sit and remotely control the robotic arms and instruments. The surgeon's hand movements are translated into precise micro-movements of the instruments, filtering out tremors and scaling motions as required.

A patient-side cart contains robotic arms to hold and exchange the tools easily. As robotic arms provide a wider range of motion and dexterity compared to human hands, they can rotate instruments in a way that allows surgery to be performed through small incisions.

The 3D vision system provides a precise view of the surgical area. It enhances depth perception and magnification, proving extremely beneficial when identifying anatomical structures and navigating complex surgical pathways. With all these components combined, this setup enhances maneuverability and accuracy of the movement, which are crucial for delicate surgical operations.

Although the da Vinci system is primarily known for its applications in laparoscopic surgery, it is also used in endoscopic procedures. One such application is endoscopic full-thickness gastric resection (EFTGR) with regional lymph node dissection (LND) for treating early gastric cancer [14, 15]. This procedure involves the da Vinci system's 3D near-infrared video technology. With its significantly enhanced visualization of the lymphatic system, surgeons can perform more precise dissection of lymph nodes, demonstrating the system's versatility and capability beyond traditional laparoscopic surgery.



Figure 2. 2 View of the setup of the patient and the da Vinci surgical robot (Images from open-access journals licensed under the Creative Commons Attribution License) [14]

A study conducted between 2015 and 2018 involved 24 patients undergoing EFTGR and LND using the Da Vinci surgical robot system. The clinical outcomes were notably

positive, with the absence of mortality or cancer recurrence of the patients over a five-year follow-up period [15]. These results underscore the da Vinci system's ability to effectively perform complex endoscopic procedures, paving the way for broader adoption and further innovation in robot-assisted surgery.

2.1.2 EndoMaster

Natural Orifice Transluminal Endoscopic Surgery (NOTES) is an innovative approach to minimally invasive surgery. Accessing internal organs through natural orifices such as the mouth and anus eliminates the need for external incisions [17, 18]. This approach reduces patients' scarring and recovery time associated with traditional laparoscopic surgery.

EndoMaster system, developed at Nanyang Technological University, is specifically designed for NOTES [19]. It integrates robotic arms with flexible endoscopes that pass through natural orifices to reach body organs [20, 21]. This approach speeds up the patient's recovery while offering enhanced maneuverability for fine tissue manipulation and dissection.

The Endomaster EASE System is an advanced flexible robotic endoscopy platform designed for endoscopic submucosal dissection (ESD) [19, 22]. The system has a remote-control console for operating the robotic arms and a separate endoscopic platform. In total, it offers nine degrees of freedom; A surgeon controls the robotic arms via the console, with the left arm focused on retraction and the right on dissection. Early animal trials demonstrated its capability to perform successful procedures such as full-thickness gastric resection, hepatic wedge resection, and ESD in the stomach and colon [23, 24]. These studies showcased the EndoMaster system's potential to achieve comparable outcomes to traditional open or laparoscopic surgeries, with additional benefits associated with NOTES.

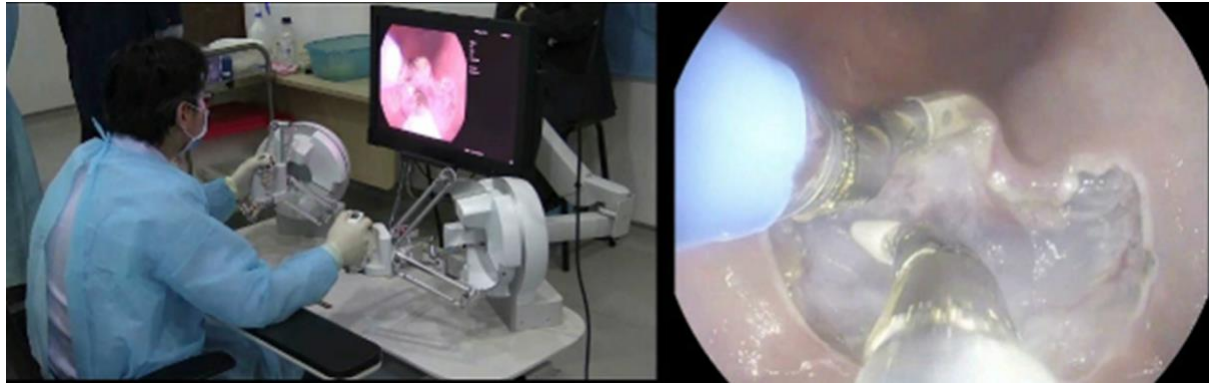


Figure 2. 3 Colonic endoscopic submucosal dissection performed using the latest version of the EndoMaster EASE System (Images are reused from open-access journals licensed under the Creative Commons Attribution License) [18]

Another application of the EndoMaster system is in transoral robotic surgery (TORS), where the head and neck region are accessed through the mouth for surgical procedures. The cadaveric study by Tay et al. (2018) demonstrates that the system provides excellent visualization and quick docking due to its compact form [25]. This allows the system to avoid the clashing of the robotic arms, which is sometimes experienced with the da Vinci surgical system in TORS [16]. The flexible endoscope allows optimal positioning of the camera and tools, although further calibration of the robotic arms is required.

The EndoMaster system presents unique advantages over robotic surgical systems like Da Vinci and Flex Robotic Systems. Its flexible endoscope offers improved maneuverability compared to the rigid endoscopes of the da Vinci, and greater agility than the non-robotic instruments of the Flex [16, 26]. It shows promising potential to be used for TORS but requires further refinements and clinical studies to optimize its performance.

In summary, the EndoMaster system represents an innovation in robotic endoscopic surgery. It opens up possibilities of conducting difficult surgeries through natural orifices at increased precision and minimizing patient trauma. Further research and clinical tests are required to enhance the system toward its full installment in practical surgery.

2.2 Tendon Sheath Mechanism

2.2.1 Mechanism of TSM

Tendon Sheath Mechanism (TSM) is an essential component in flexible surgical robots. The mechanism comprises a tendon, a metal wire, that passes through a flexible wound wire coil used as a sheath [27]. When the tendon is pulled at one end, it transmits force and displacement toward the opposite end. This bears a close resemblance to natural tendon-sheath structures in the human body, such as the remote actuation of joints in the fingers. TSM allows power sources and actuation motors to be placed outside while transmitting force and energy to the robot at the distal end [28].

TSM modeling captures various factors such as friction, compliance, and bending of the sheath to comprehend the interaction between the tendon and the sheath. The force transmission in TSM can be described using a capstan equation, which characterizes an exponential relationship between the input and output tensions due to friction over a curved surface [29]:

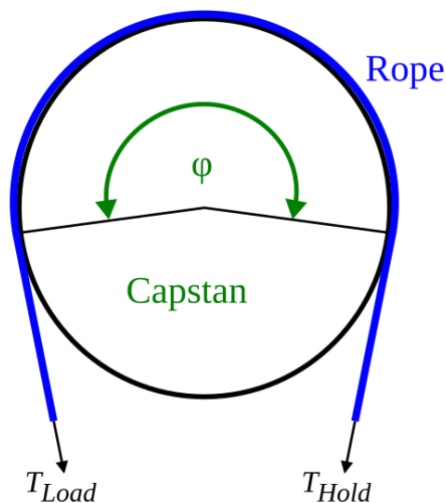


Figure 2. 4 "Capstan equation diagram" by Krishnavedala is licensed under the Creative Commons Attribution License

$$T_2 = T_1 e^{\mu\varphi}$$

$T_1 = \text{Input Tension, N}$

$T_2 = \text{Output Tension, N}$

$\mu = \text{Coefficient of friction between the tendon and sheath}$

$\varphi = \text{Total bending angle of the sheath, }^\circ$

In a curve configuration, the equation demonstrates that friction increases exponentially with a bending angle; a small increase in total bending angle is enough to create a significant impact on force transmission.

Another important aspect of TSM modeling is accounting for elastic deformation of both the tendon and the sheath. When under a load, tendon and sheath can stretch and consequently affect the accuracy of both force and displacement transmission. Hooke's law describes the elongation, δ , created due to an applied force, F :

$$F = k\delta$$

$$\delta = \frac{F}{k}$$

$F = \text{force Applied (Load), N}$

$k = \text{Stiffness coefficient, N/m}$

$\delta = \text{Elongation due to an applied force, m}$

This suggests that for a stiffer tendon sheath, the elongation is shorter and hence preferable for a finer control [B35].

TSM also exhibits hysteresis and backlash due to nonlinear frictional forces and material compliance. These nonlinearities produce energy losses and positional errors that interfere with the precise control of a robotic end effector [30]. Hysteresis is usually presented as a difference in the force-displacement relationship during loading and unloading cycles, giving rise to the time lag between input and output motions.

Understanding these phenomena is crucial for developing appropriate control algorithms that compensate for the nonlinearities observed in the TSM. Accurate modeling enables predictive control strategies to predict friction and compliance effects, enabling the performance of a surgical robot to improve.

2.2.2 Control Challenges in TSM-Driven Mechanism

Controlling the robots driven by TSM involves a few difficulties arising from the mechanism's intrinsic nonlinearities. Nonlinear friction between the tendon and sheath depends on bending angles, tension, and environmental conditions. These may cause a difference between input commands and real end-effector motions, making the system unpredictable [32]. In addition to hysteresis caused by friction, more difficulties arise due to compliance of the tendon and sheath [33]. The elastic properties of tendons and sheaths can cause delays in force transmission as the system response is not linear to the input forces [34]. This compliance could be further altered with temperature and wear, making the system more complex.

To handle these issues, researchers have applied different control methods, namely friction compensation techniques. For example, a dynamic friction model like the LuGre friction model captures various frictional behaviors such as pre-sliding displacement, frictional lag, etc, for the improved estimation of frictional forces [35]. Through such models, the control systems can change the commands of actuators to counteract friction-induced errors.

Next, adaptive control strategies are employed, where control parameters are updated in real-time based on the feedback received from the system itself [36]. One advantage of such an approach is that it adapts to the changes caused by friction, compliance, or external disturbance in the behavior of the TSM. This allows constant tuning of the control parameters, improving overall performance and minimizing errors.

Robust control techniques are another example of how the system further boosts its performance with uncertainties and modeling inaccuracies. It develops techniques for guaranteed stability and performance within the specific bounds, but without necessarily knowing the parameters of the exact setup.

2.2.3 Haptic Feedback

Haptic feedback is invaluable in robotic-assisted surgeries for improving surgical accuracy, reducing tissue damage, and mitigating operator fatigue [39-40]. Through the connected sensations concerning the forces experienced by the robotic instruments, the surgeon can manipulate the tissues in a controlled manner. Without it, the surgeon has to rely heavily on visual and experiential information. The most important feedback information includes tissue properties, obstruction detection, and current pressure capacitance [41].

Space constraint of TSM, however, hinders the direct measurement of the distal-end force. Installing force sensors at the distal end enlarges the size and possibly the complexity of the instruments, too. As a result, indirect methods for estimating distal forces are developed as alternatives.

One such method is proximal force sensing. It measures the forces at the actuator end and uses the measurements to estimate distal end forces using mathematical models [42]. Early

models, such as Kaneko et al., employed lumped mass models with Coulomb friction to estimate tension loss [43-44]. Subsequent models incorporated dynamic aspects, nonlinear hysteresis, and complex parameter identification processes.

Recent efforts have utilized machine learning to improve force estimation. A study by S.J. Phee et al. introduces a two-stage data-driven solution to predict distal-end forces without prior knowledge of sheath configuration [8]. The first stage uses the convolutional neural network (CNN) to estimate the sheath's cumulative bending angle based on proximal-end force responses to a probing signal. The CNN analyzes patterns in the sensor data to infer the configuration of the TSM without any explicit geometric measurements.

The second stage combines two long short-term memory (LSTM) models, pre-trained for the nearest estimated bending angles, to dynamically estimate distal-end forces. The LSTM networks have been utilized in modeling the hysteretic effect and compliance of the TSM, owing to their great capability to learn temporal dependency and nonlinear relationships from sequential data.

The study exhibits that the machine learning approach is compatible with many force hysteresis profiles and does not require any prior information about the sheath configuration, while accurately identifying hysteresis phases [8]. This makes it suitable for surgical applications where the sheath shape can change unpredictably. The system enhances haptic feedback by providing more accurate force estimations, hence improving the ability of the surgeon to carry out delicate procedures.

2.2.4 Home Positioning

"Home positioning," the capacity to precisely and consistently place the surgical instruments at a pre-determined reference point, is a key concept in endoscopic robotic surgery. This guarantees that the system can reliably return to its initial state, making it easier for surgeons to perform difficult procedures [47, 10]. Therefore, dependable home positioning is crucial for safe and efficient surgical procedures.

Home positioning in TSM-driven systems is complicated by nonlinearities introduced due to friction and compliance. Friction may prohibit the tendon from fully returning to its exact initial position, while compliance may lead to residual deformations that affect positioning accuracy [48]. These are some of the factors that create uncertainties in the instrument's actual position relative to the intended home position.

Despite advancements in robotic surgery, there remains a notable gap in endoscopic robotic systems: lack of control algorithms for reliable home positioning. The challenges in control come from the tendon elongation and non-linear friction along the long flexible TSM. The traditional home positioning is based on a manual adjustment that utilizes sensors, like encoders, which track the position of the actuators [49]. However, these methods can be imprecise due to the flexibility and variability of endoscopic paths [51].

2.3 Robotic Grippers

2.3.1 Design and Kinematics of Robotic Grippers

The robotic grippers in endoscopic surgery allow manipulation tasks such as grasping, cutting, or stitching within the highly confined human body. Such grippers have to be designed with great caution to meet the higher demands of minimal invasiveness.

Firstly, the grippers should be miniaturized to fit into the limited diameter of endoscopic tools, which typically range from 2 to 5 millimeters [52]. Such miniaturization usually complicates the integration of mechanical components and degrees of freedom within such a form factor. Materials and manufacturing techniques should be chosen with durability and biocompatibility in mind but without hindering functionality.

Secondly, the grippers must be dexterous to enable multi-degree-of-freedom (DOF) movement in performing complicated manipulation of tissues effectively [53]. Dexterity at a high degree necessitates the design of sophisticated linkage mechanisms and joints that could avail several DOFs with structural integrity [54]. In design, a balance must be obtained between flexibility and precision on one hand and size and strength on the other.

In the kinematic modeling of robotic grippers, DOF should be defined in relations between joint movements and end-effector positions. D-H parameters generally use mathematical modeling for kinematics, which describes the geometry of a robotic manipulator [55-56]. The modeling is essential for developing control algorithms and precisely positioning and orienting the gripper.

The D-H convention ensures that each joint and link within the gripper is assigned parameters that describe its relative position and orientation. One can then calculate the forward

kinematics, which will determine the position and orientation of the gripper tip from the joint variables. In parallel, inverse kinematics will identify what movements of the joints must occur to achieve any desired end-effector's position.

2.3.1 Force Transmission in TSM-Driven Grippers

Effective force transmission is crucial for robotic grippers to apply an adequate magnitude of forces for grasping tissues without causing damage. In TSM-driven systems, the force applied from an actuator should be effectively transmitted through the tendon-sheath mechanism to the gripper.

The mechanical advantage of the gripper defines the ratio of output force at the jaws to input force provided by the actuator [57]:

$$MA = \frac{F_o}{F_i}$$

$MA = \text{Mechanical Advantage}$

$F_o = \text{Output Force}$

$F_i = \text{Input Force}$

Grippers must be designed with an appropriate mechanical advantage that ensures sufficient force while putting as little as possible in input. In addition, friction and compliance influence the efficiency of force transmission. Friction can decrease the effective force transmitted, and compliance may cause energy loss through elastic deformation [58]. These factors suggest that the actual output force achieved is far below the estimated value, based on mechanical advantage alone.

To address these problems, materials with lower friction coefficients are used for tendons and sheaths. In addition, in some applications, pre-tensioning the tendon reduces slack and increases responsiveness. Being able to comprehend and compensate for such factors is an important aspect of designing grippers.

2.3.2 Robotic Gripper Control

Various control strategies of the robotic grippers have been implemented to achieve fine manipulation and safety during the surgeries. One of the strategies is impedance control, in which the dynamic relationship between the position error of a manipulator's end-effector and the force of interaction with the environment is used to achieve the desired impedance [59]. Desired impedance behavior can be represented by the following equation:

$$F_{ext} = M_d \ddot{x} + B_d \dot{x} + K_d x$$

F_{ext} = External Force, N

M_d = Desired Inertia

B_d = Desired Damping

K_d = Desired Stiffness

x = Position of the Gripper

The three parameters above ensure that compliant behavior can be achieved by choosing them appropriately in a control system. By controlling impedances, the gripper will adapt to soft and hard tissues seamlessly. For example, in the grasping of fragile tissues, a compliant behavior will prevent excessive application of forces, reducing the possibility of further damage.

Another approach is admittance control, wherein the motion of the gripper is governed by sensed forces. It is thus appropriate in environments where a high degree of precision in force control is paramount [60]. In an admittance control, the control system interprets the external forces and commands motions to achieve the desired interaction. Admittance control is especially beneficial when the gripper must follow external forces, such as while manipulating tissues that exert reactive forces. When forces are sensed, the gripper responds appropriately and keeps contact without applying excessive force.

These control strategies involve feedback from sensors, such as force or torque sensors. The input of the sensors within the control algorithms enables the robotic gripper to respond to changes in the dynamic surgical environment, enhancing both performance and safety.

3. METHODOLOGY

3.1 System Overview

The project focuses on developing a control algorithm for the home position tuning of endoscopic surgical robots. Although a full endoscopic surgical robot is not incorporated into the project, a separate model is designed to simulate the concept of home position tuning. The main components of the model include a proximal and distal pulley, TSM, Dynamixel-106 motor as the actuator, and a control unit. The design aims to replicate the flexibility and complexity of endoscopic surgical robots.

3.2 Home Position Tuning Approach

The home position tuning approach aims to accurately calibrate the starting position of a robotic end-effector, ensuring precise control and effective operation. In this experiment, motor current readings will be used to improve home positioning accuracy. This is because the motor current relates directly to the torque applied by the actuator and hence provides information on the resistance encountered by the end effector [B51]. In endoscopic surgical scenario, when the robotic gripper touches the endoscope's channel, it triggers an increase in motor current, thus giving a signal for control adjustments.

In this study, motor current acts as a means to gain information required by the control algorithms, on whether the instrument has reached its limit or home position in the presence of nonlinearities. Through this method, one could implement a stall detection algorithm whereby a significant increase in current suggests that the motor is using torque without movement, hence the end effector, the robotic gripper, has reached a limit. The approach comprises the following steps:

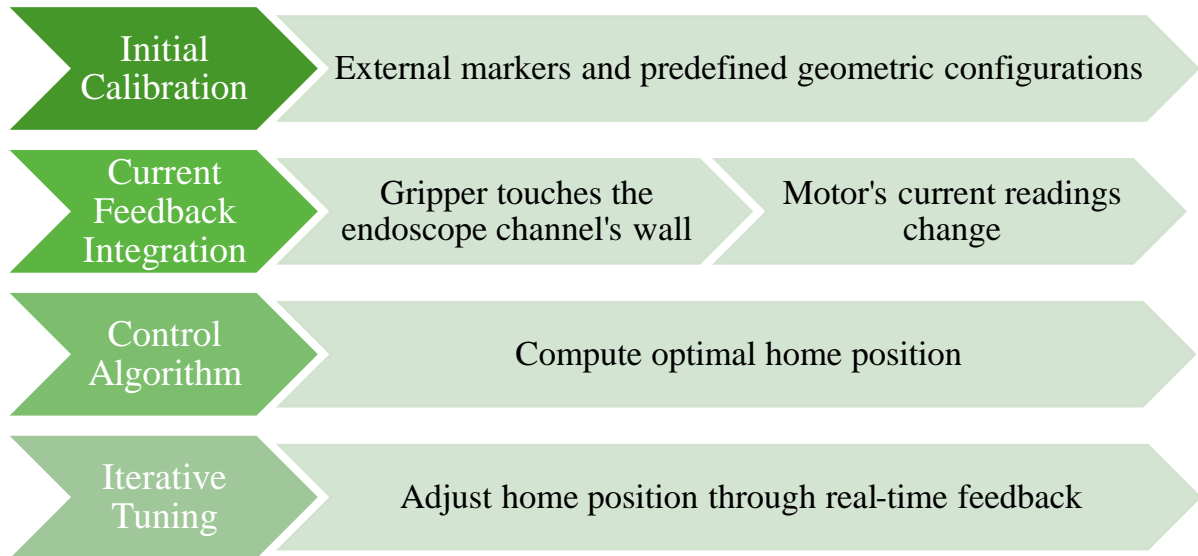


Figure 3. 1 Home Position Tuning Steps

Moreover, real-time compensation using motor current readings empowers the control system to refresh the actuator commands dynamically owing to friction and compliance variations accordingly [52]. These adaptive algorithms may automatically adjust the control inputs in response to changes in the system to ensure continued performance through some references.

These strategies, when implemented, enhance the reliability of home positioning and reduce manual adjustments. It compensates for nonlinearities occurring in a TSM and improves safety and efficiency during the performance of a surgical procedure; hence, the overall effectiveness of robotic-assisted surgery is thereby boosted.

3.3 Experimental Setup

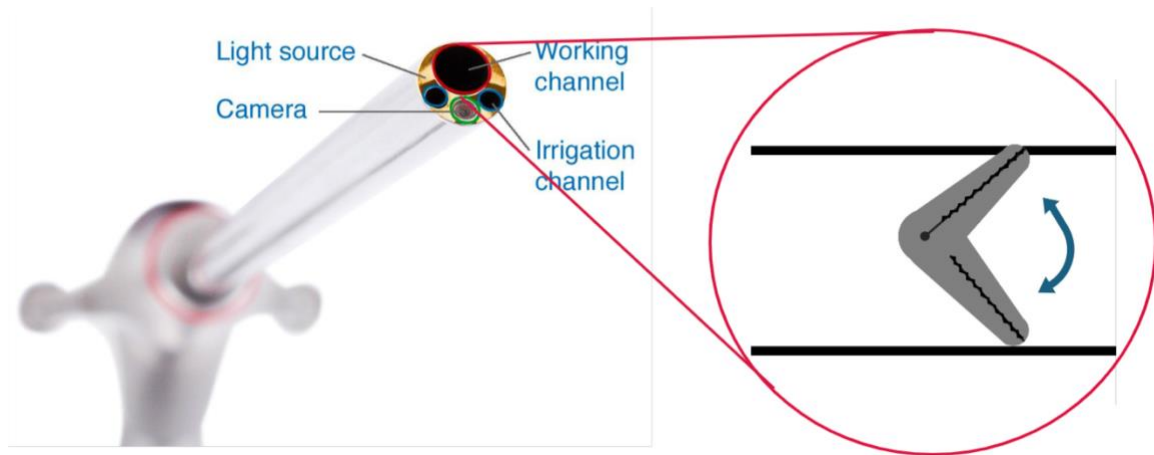
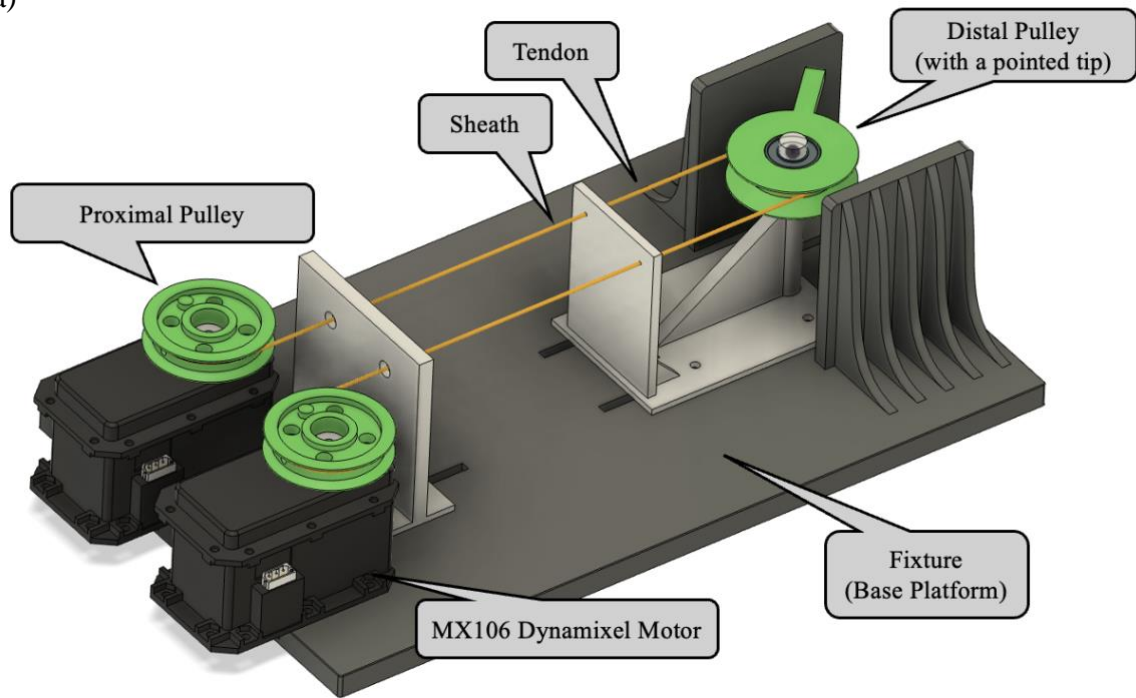


Figure 3. 2 Gripper Inside Endoscope Channel

The experimental setup is designed to replicate the environment of endoscopic surgical robots. TSM involves physical tendons and sheaths, where a metal wire (tendon) passes through a hollow coil (sheath) 1 meter long. This length reflects the extended pathways within the endoscopic system, where tendons must go through intricate anatomical routes.

At the distal end of this setup, a pulley with a pointed tip is installed to mimic the action of a robotic gripper inside the endoscope's channel. The pointed tip of the pulley is designed to turn right and left, simulating the robotic gripper touching the endoscope's channel walls as demonstrated in Figure 3.2. This movement is crucial for detecting the angle of contact points, which are required for computing the home position.

(a)



(b)

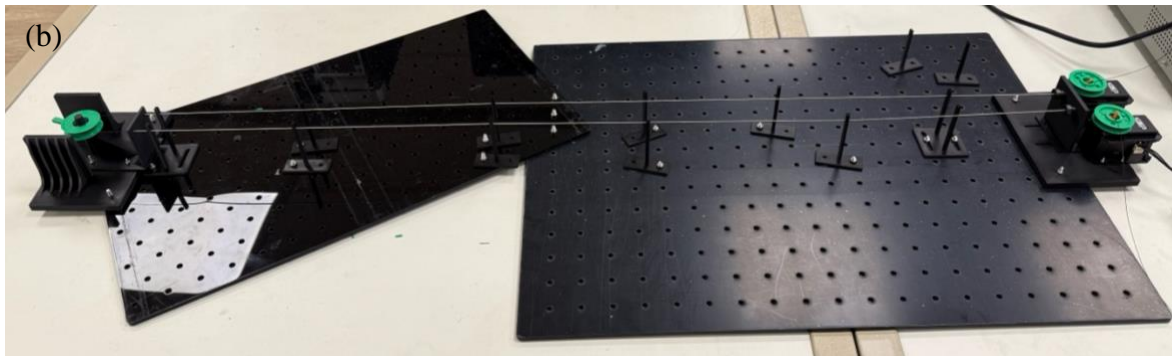


Figure 3. 3 (a) CAD Experiment Setup (b) Actual Experiment Setup

The tendons are driven by DC motors, MX106 Dynamixel. The motors control the tension in the tendons, adjusting the position and movement of the distal pulley. When the tip touches an obstacle, the resistance of the motor increases, causing a spike in the current. This current feedback from the motors is then used to detect the angle at which the pointed tip of the pulley touches the channel walls.

To investigate the performances of the home position tuning algorithm in various conditions, the sheath is arranged in the following configurations:

- **Straight Configuration:** The sheath is laid straight, outlining the minimum curvatures and friction, serving as the simplest travel route. This sets a baseline performance.

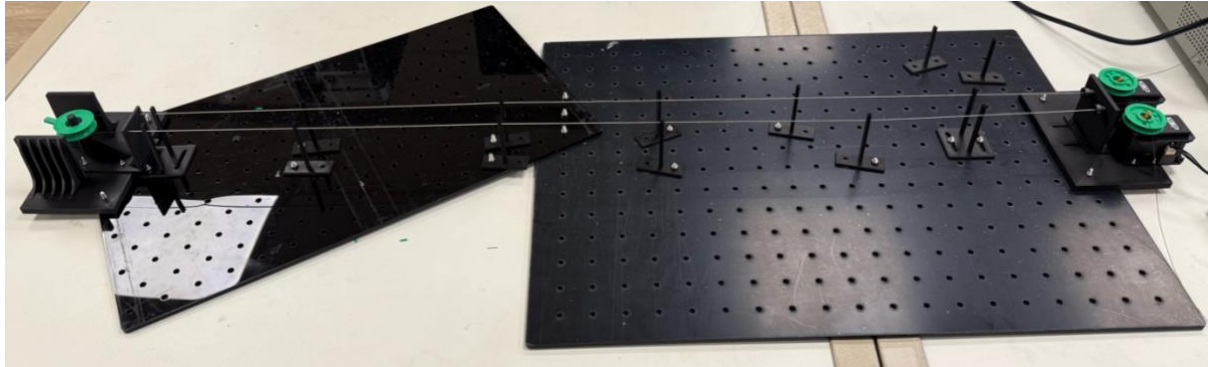


Figure 3. 4 Straight Configuration

- **Curved Configuration, $\sin(\frac{1}{2}x)$:** The sheath is arranged in curves along its entire length, forming a half-sine wave. Here, one introduces a medium level of curvature. This setup replicates common bends an endoscope could take while negotiating through its pathway in the human body. This setup adds more complexity due to increased friction and nonlinearities in tendon-sheath interaction.

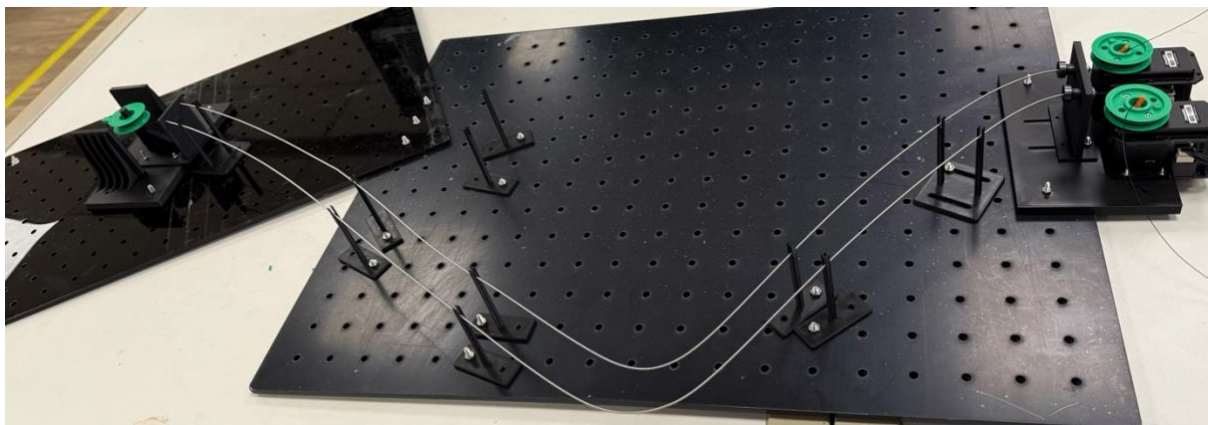


Figure 3. 5 Curved Configuration, Sin(0.5x)

- **Curved Configuration $\sin(x)$:** The sheath forms one full sinusoidal shape with larger amplitude bends. Such a configuration should depict a highly curved course of flight and therefore give a higher friction value, challenging the algorithm to make greater nonlinear compensations.

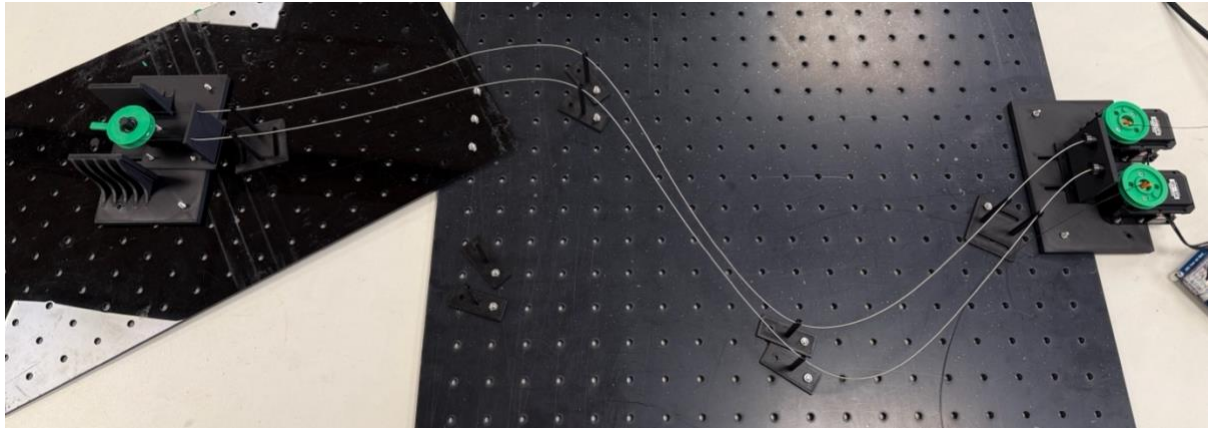


Figure 3. 6 Curved Configuration $\sin(x)$

In addition to these varied configurations, the angle at which the distal-pulley's tip contacts the wall is also diversified into three kinds. This is to ensure that the control algorithm is tested in a dynamic environment, a closer representation of actual surgical environment. As displayed in Figure 3.7, the position of distal pulley is adjusted 10mm, 20mm, and 30mm away from the edge, resulting in different contact angles of 52.7° , 53.3° , and 53.9° respectively.

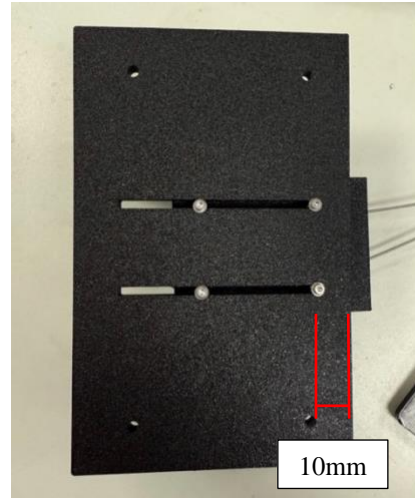
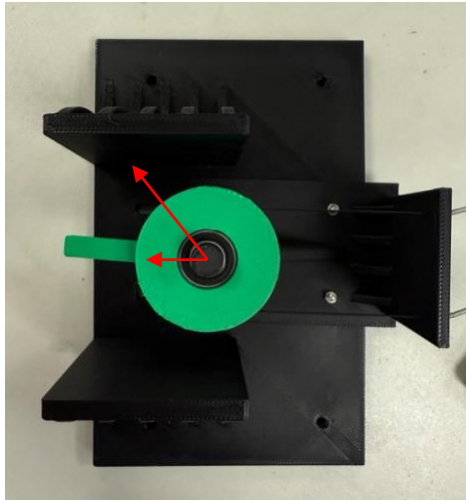
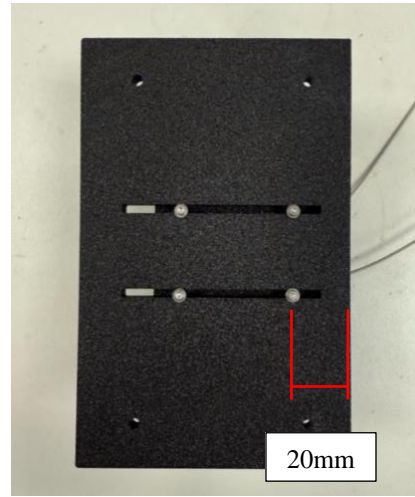
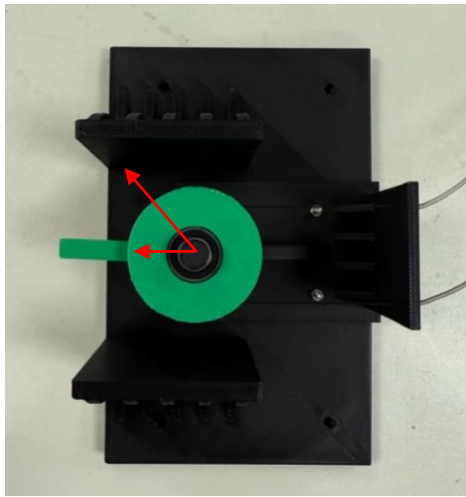
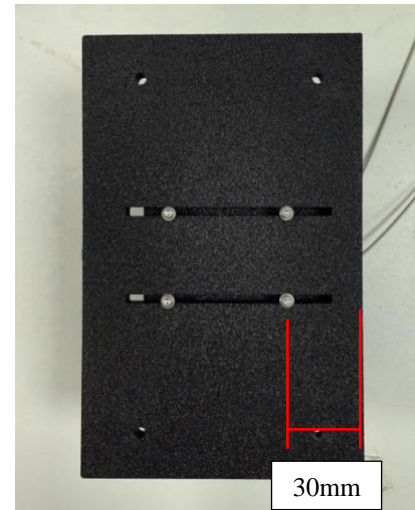
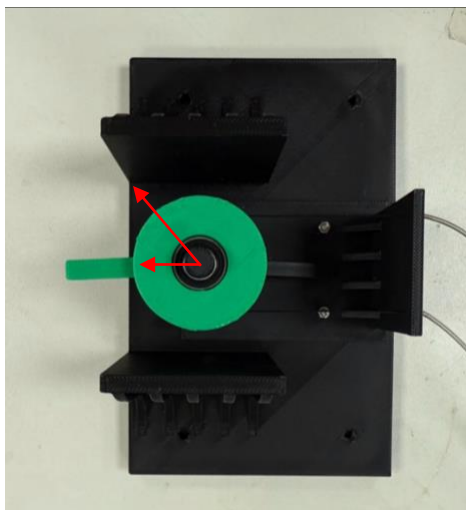


Figure 3. 7 (a) Smallest Contact Angle, 52.7°



(b) 20mm – Middle Contact Angle, 53.3°



(c) 30mm – Largest Contact Angle, 53.9°

Next, a computer system is integrated into the setup for data acquisition and analysis. It captures the current feedback from the MX106 Dynamixel motor and uses a control algorithm to compute the optimal home position. The experimental setup combines mechanical precision with data analysis to develop an effective home position tuning mechanism for endoscopic surgical robots.

3.4 Data Collection and Analysis

Data collection involves capturing current feedback from the MX106 Dynamixel motors as the distal pulley rotates. The entire home positioning process is conducted in two phases: the initial calibration phase and the tuning phase. During the initial calibration phase, the motor's current is recorded to establish its baseline. Next, as the tip of the pulley touches the wall, current feedback is continuously captured to monitor the change. These comprehensive data collection procedures ensure a reliable dataset required for the control algorithm.

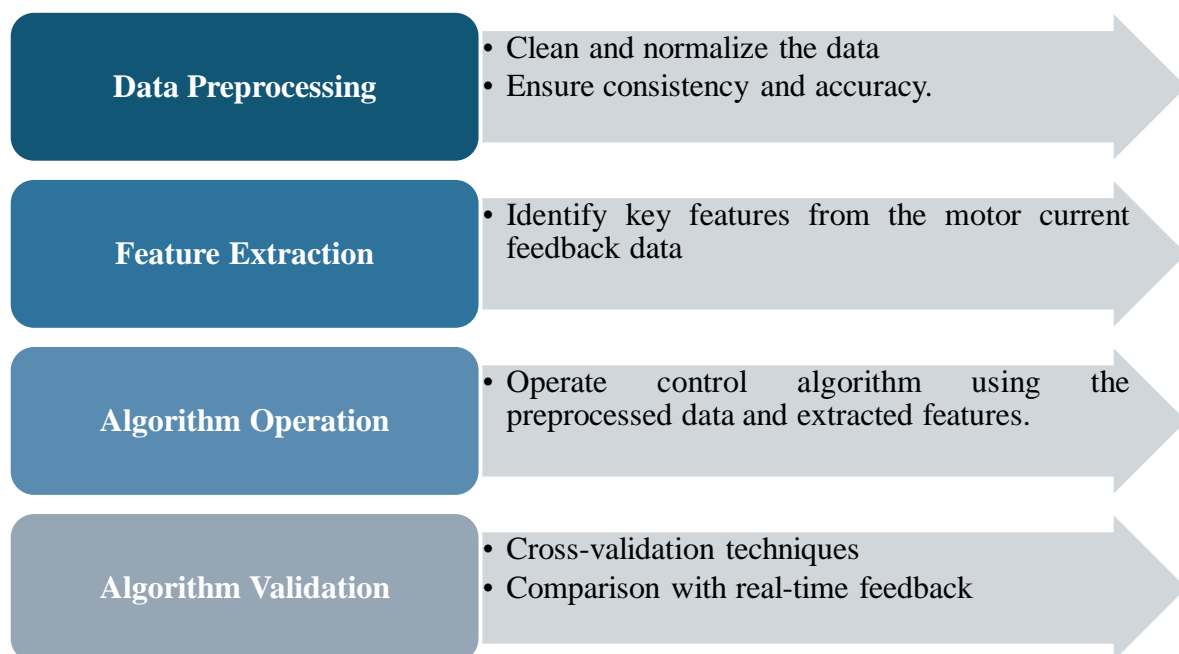


Figure 3. 8 Data Collection and Analysis Flowchart

4. IMPLEMENTATION

4.1 Hardware Implementation

4.1.1 MX106 Dynamixel Motor

The MX106 Dynamixel motor (Protocol 2.0) is a servo motor that precisely controls angular position, speed, and torque. It can be operated in a current-based position control mode, which is a primary reason for its selection in this project. This mode is instrumental in detecting the contact points between the pulley tip and the endoscope's channel wall by monitoring the changes in current. The ability to finely control the motor's position based on current feedback allows precise tuning of the tendons' tension, ensuring accurate home position calibration.



Figure 4. 1 MX106 Dynamixel motors [61]

Following is the technical specification of MX106 Dynamixel(2.0) that aligns with the demands of this project:

- **High Torque Output:** The motor provides 8.4 Nm of maximum stall torque at 14.8 V operating voltage. It is capable of overcoming friction and mechanical resistance inside the TSM.
- **Speed:** It achieves a no-load speed of 45 RPM, allowing fast positional adjustments, which are necessary during a surgical procedure.

- **High Resolution:** It includes a resolution specification of 4096 positions per revolution, approximately 0.088 degrees per step. This equips the motor to provide accurate angular movements.
- **Communication Protocols:** These include both TTL and RS-485 communication interfaces. These ensure reliable and robust data transmission. RS-485, in particular, has the advantage of being immune to noise and is capable of long-distance communication, which is quite useful in complex robotic systems.
- **Daisy-Chaining Capability:** Multiple MX-106 motors can be daisy-chained with a single communication line to reduce wiring and simplify integration in the robotic system. Two MX-106 motors are daisy-chained for this project.

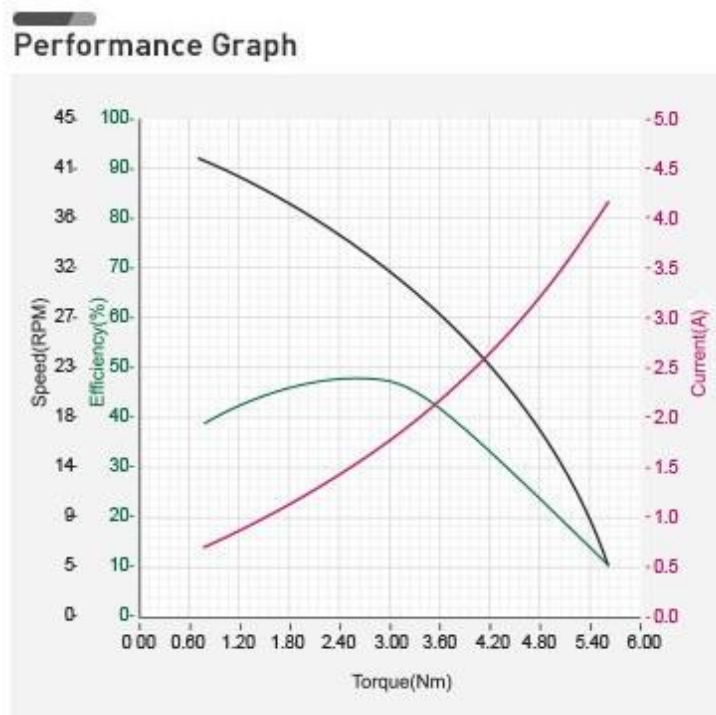


Figure 4. 2 MX106 Dynamixel performance chart

The performance graph of the MX106, or N-T curve, demonstrates its capability under conditions that simulate a gradually increasing load. While the stall torque represents the maximum momentary torque output, the performance graph in Figure 4.2 provides a more

realistic measure of the continuous output rating and expected performance in real-life applications. The maximum torque shown in the performance graph is typically less than the maximum stall torque, which is why the performance graph is widely used in the industrial field.

Through the performance graph, the following information is obtained:

Input Voltage	12V
Current	1.6A
Torque	2.7Nm
Efficiency	48%

This allows us to find the mechanical power and eventually the speed of the motor. The formula that relates electrical and mechanical power is as follows:

$$P_{out} = \eta \times P_{in}$$

$$P_{out} = \eta \times I \times V$$

$$P_{out} = \tau \times \omega$$

$$P_{out} = \tau \times N \times \frac{2\pi}{60}$$

$$P_{out} = \text{Mechanical Power Output, } W$$

$$P_{in} = \text{Mechanical Power Input, } W$$

$$\eta = \text{Motor efficiency, \%}$$

$$\tau = \text{Torque produced by motor, Nm}$$

$$\omega = \text{Angular velocity of the motor, rad/s}$$

$$N = \text{Angular velocity of the motor, rpm}$$

Using the N-T curve and motor specification, the motor torque constant, K_t , is calculated with the following equation:

$$K_t = \frac{T_{stall}}{I_{stall}}$$

With motor specifications:

$$T_{stall} = 8.4 \text{ Nm}, \quad I_{stall} = 6.6 \text{ A}$$

$$K_t = \frac{T_{stall}}{I_{stall}} = \frac{8.4 \text{ Nm}}{6.6 \text{ A}} = 1.27 \frac{\text{Nm}}{\text{A}}$$

4.1.2 Distal Pulley & Bearing

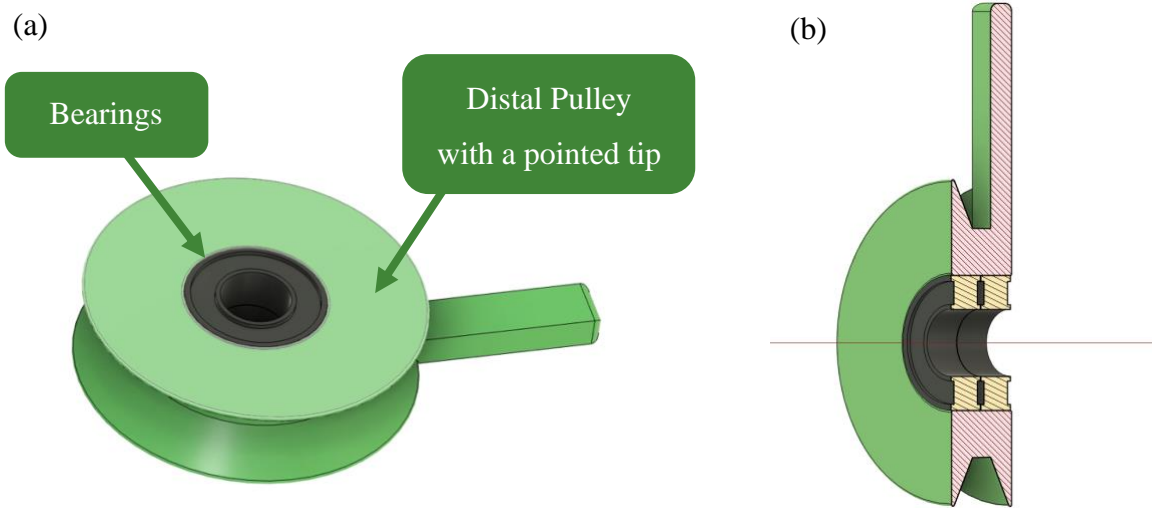


Figure 4. 3 (a) Distal Pulley with a pointed tip & Bearings (b) Cross-sectional view of distal pulley and bearings

The distal pulley, equipped with a pointed tip, mimics the robotic gripper inside the endoscope's channel. The pulley is 3D printed using Acrylonitrile Butadiene Styrene (ABS), a material popular for its strength and durability. The pulley will be turned right and left, simulating how a robotic gripper touches the walls of the endoscope's channel. In the middle of the pulley, two ball bearings will be installed.

These bearings facilitate smooth rotation of the pulley, resulting in a negligible amount of bearing friction torque T_b of $8.24 \times 10^{-7} Nm$ as calculated below:

$$T_b = f_b \times F_r \times r_b$$

$$F_r = 0.007 \text{ kg} \times 9.81 \text{ m/s}^2 = 0.0687N$$

$$T_b = 0.0015 \times 0.0687N \times 0.008m$$

$$T_b = 8.24 \times 10^{-7} Nm$$

Bearing friction coefficient, $f_b = 0.0015$ (ball bearing)

Radial load on the bearing $F_r = m_p \times g$

Bearing radius, $r_p = 8mm = 0.008m$

Mass of pulley, $m_p = 7g = 0.007 \text{ kg}$

4.1.3 Slidable Wall

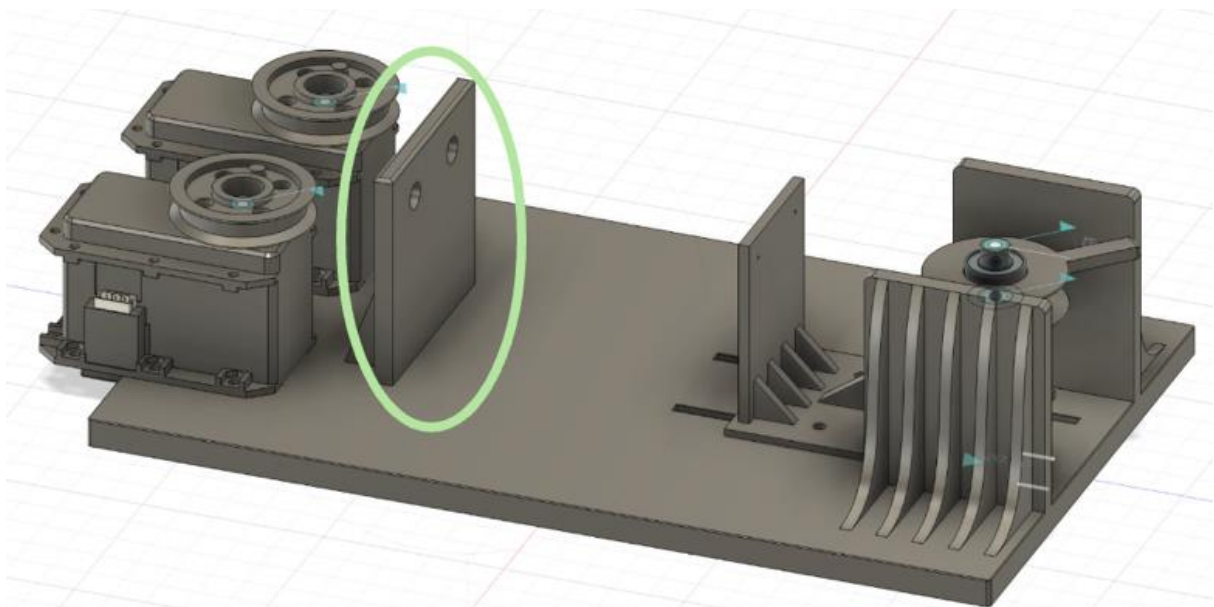


Figure 4. 4 Prototype No. 1 with attached wall

In the initial design, the wall for the tendon and sheath was non-detachable and firmly attached to the platform. This fixed configuration lacked a stepped hole, which resulted in poor positioning of the tendon and sheath. Moreover, the inability to modify the distance between the walls restricted the setup's versatility, as it could not effectively accommodate sheaths of varying lengths. This design constraint hindered the testing and validation of control algorithms under different conditions.

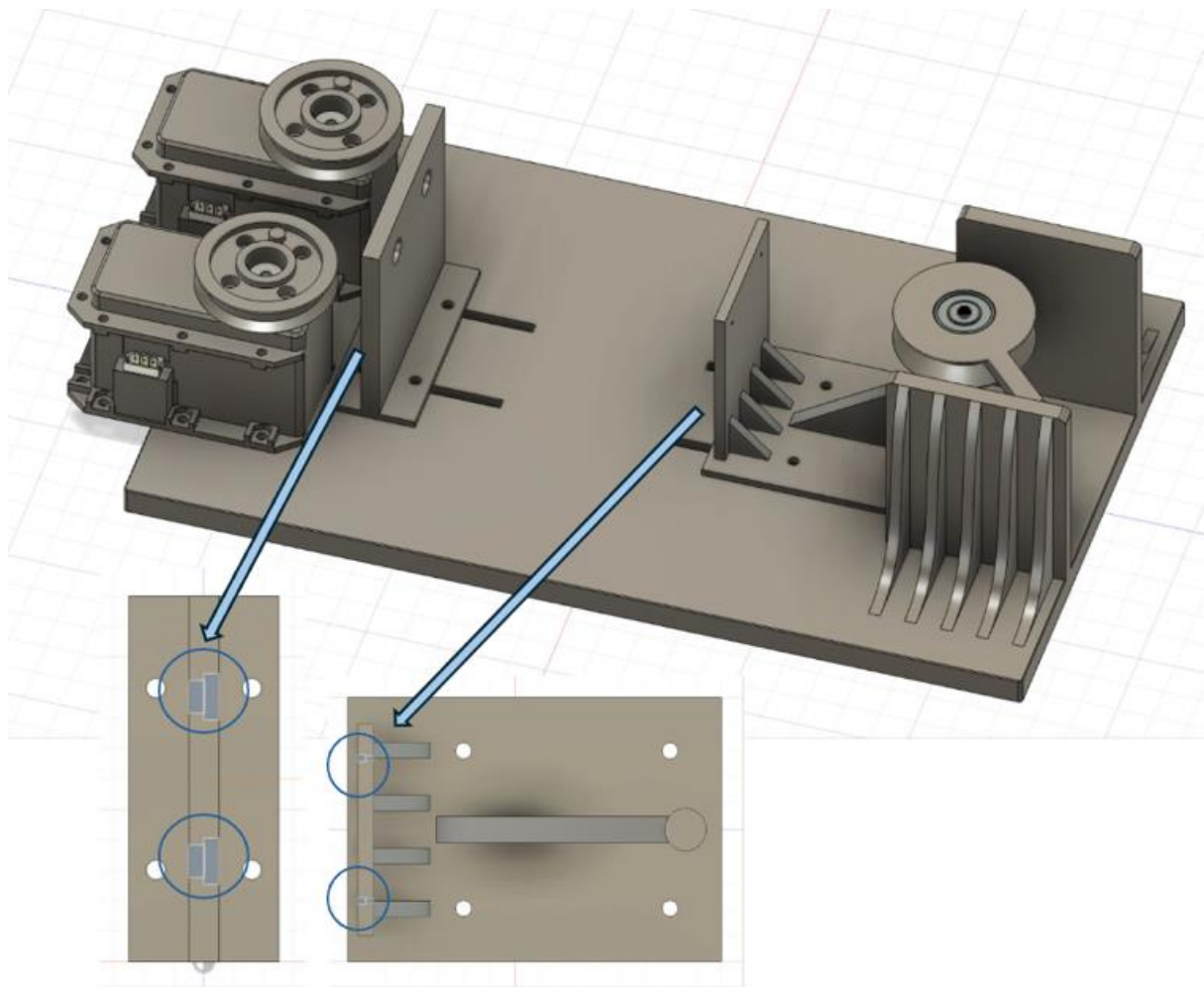


Figure 4. 5 Prototype No. 2 with detachable wall equipped with step holes

To address these limitations, a new prototype is introduced: a detachable and slidable wall equipped with step holes. This enhancement ensures secure tendon and sheath placement

while allowing the distance between two walls to be adjusted. Also, the detachable feature allows for quick adjustment of the setup. As the improved design makes it possible to accommodate sheaths of various lengths, it enhances the prototype's practicality and versatility for diverse circumstances.

Next, the prototype is further modified by splitting the base platform in half and fixing those parts to a large mounting board, as displayed in Figure 4.6 (a). This modification is required to accommodate the sheath of longer length. After the split, the motors and the end effector side are approximately 1.5m apart, providing space for the sheath to be arranged in different configurations. Several 3D-printed sheath-holders shown in Figure 4.7 are also added to the setup to ensure that sheaths are aligned to the step hole and pulley, preventing any sagging.

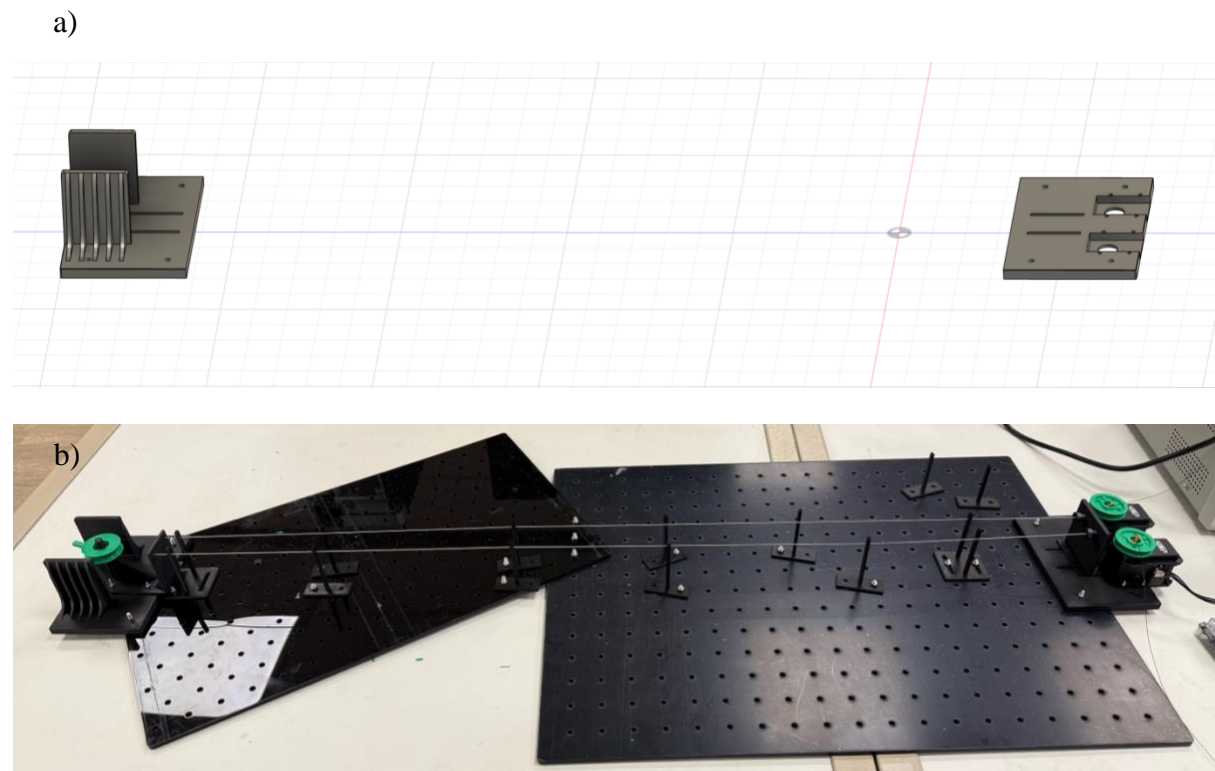


Figure 4. 6 (a) CAD model of the prototype's base (b) Real setup of the prototype on a mounting board

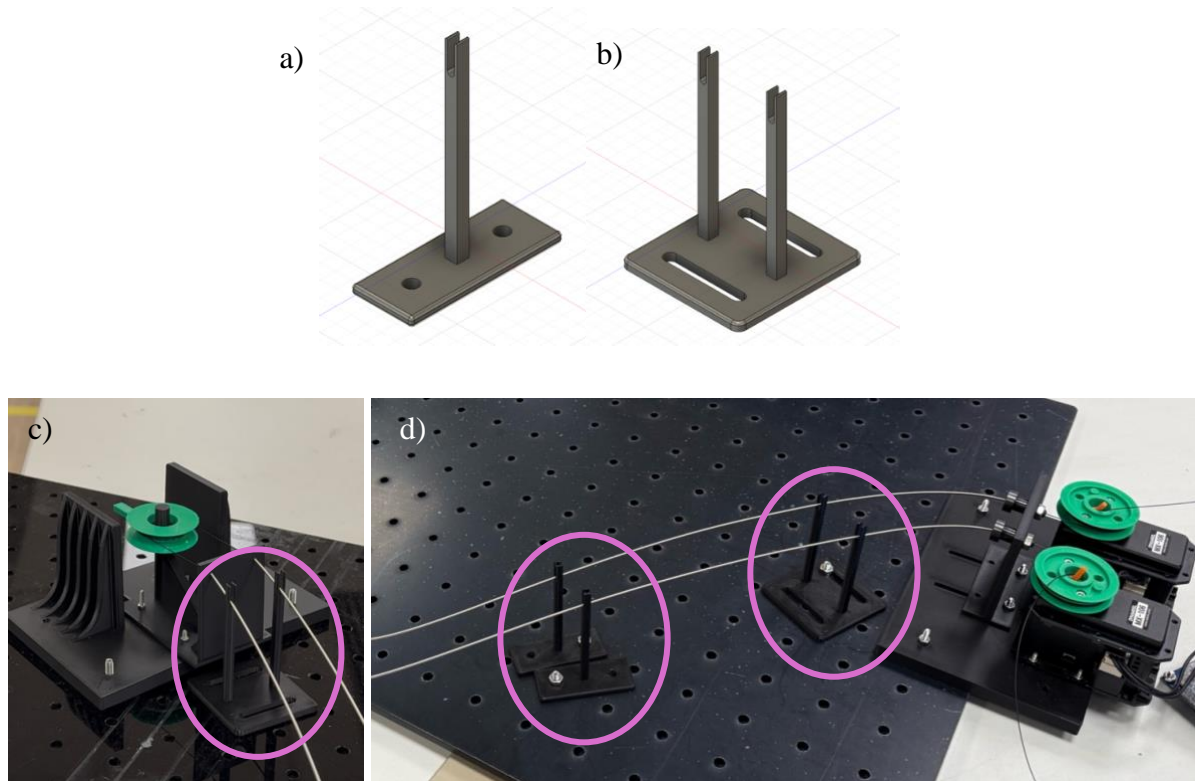


Figure 4. 7 (a) Sheath-holder type A (b) Sheath-holder type B (c) Type A near distal pulley (d) Type A&B near motors

4.2 Software Implementation

As demonstrated in the flowchart below, the flow consists of several key algorithms that process the motor's current feedback and compute the gripper's home position.

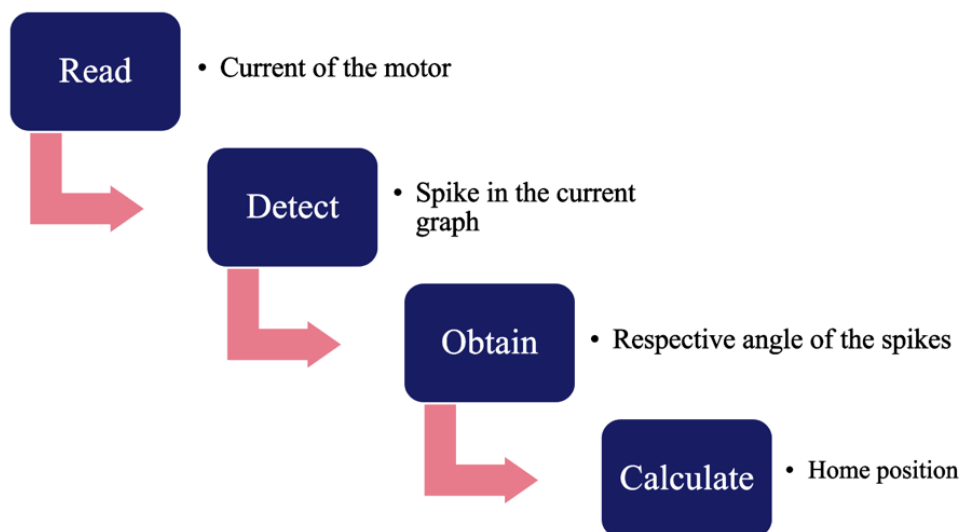


Figure 4. 8 Code Flow

4.2.1 Two's Complement

Initially, the current feedback from the motor was highly erratic as demonstrated in Figure 4.9. The readings fluctuated between one-digit and five-digit numbers, rendering data unusable for detecting meaningful peaks. This issue was resolved by implementing an algorithm that converts numbers from a two's complement format to a decimal format.

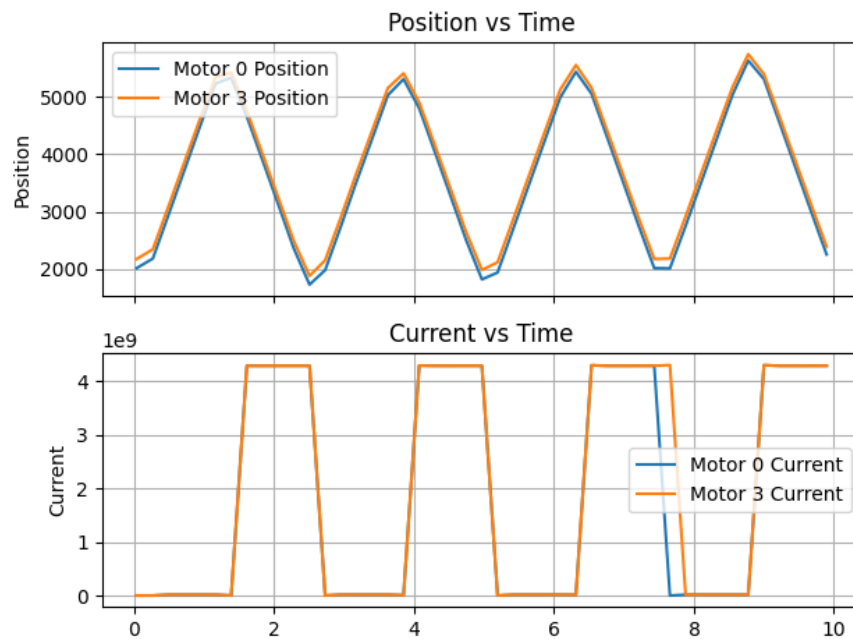


Figure 4. 9 Motor's current feedback before implementing the number conversion algorithm. Hence, the readings are highly erratic.

Two's complement method represents signed integers in binary form. For a 16-bit number, the most significant bit (MSB) indicates the sign: 0 is for positive and 1 is for negative. The steps for the conversion process are:

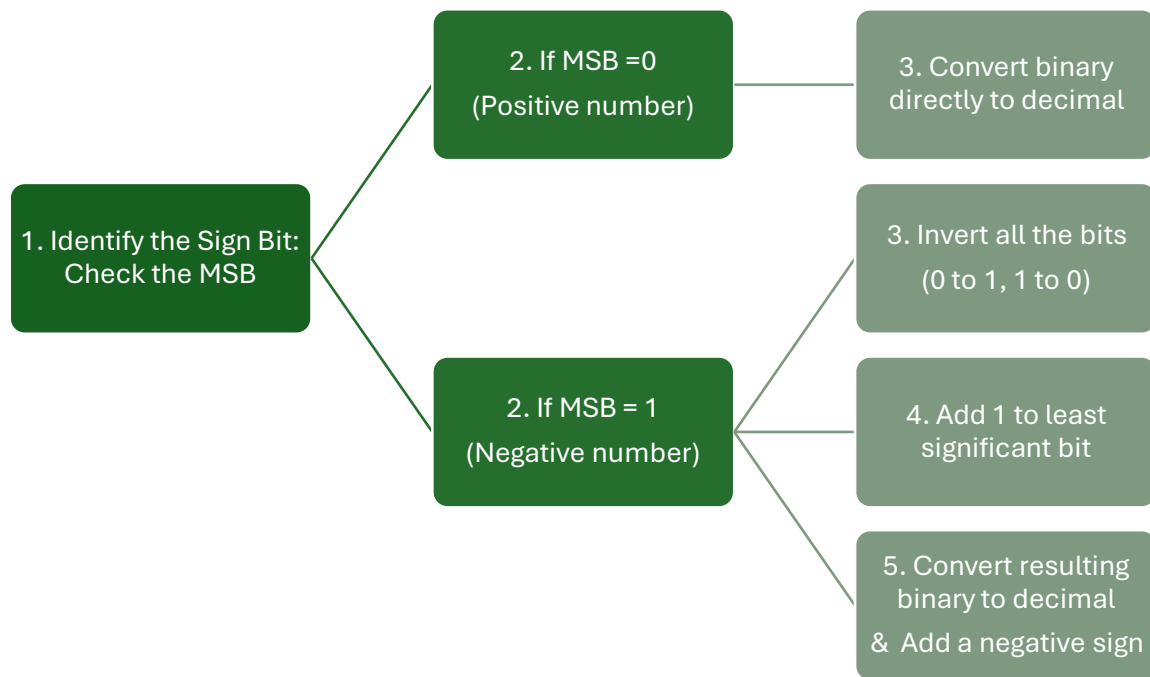


Figure 4. 10 Two's Conversion Flowchart

For example, consider a 16-bit binary number:

Binary: 11111 11001 10000 1111

Step 1: Identify the MSB (1, indicating a negative number).

Step 2: Invert all the bits: 00000 00110 01111 0000

Step 3: Add 1: 00000 00110 01111 0001

Step 4: Convert to decimal: 00000 00110 01111 0001 → 441

Since it is a negative number, the result is -441.

As the method displayed above, the raw data of the current are first converted into decimal format. Next, they are represented in milliamperes (mA) on the graph, allowing the variations in current to become more detectable and analyzable.

4.2.2 Moving Average Filter

Despite the conversion, the current feedback continued to exhibit considerable fluctuations. As a solution to this problem, an algorithm for moving the average filter was implemented. The moving average filter smooths the data by averaging surrounding data points within a window frame, reducing noise and highlighting the underlying trend. The equation for the moving average filter is as follows:

$$MA_t = \frac{1}{N} \sum_{i=0}^{N-1} x_{t-i}$$

MA_t = moving average at time t

N = window size

x_{t-i} = current value at the $(t - i)$ th time point.

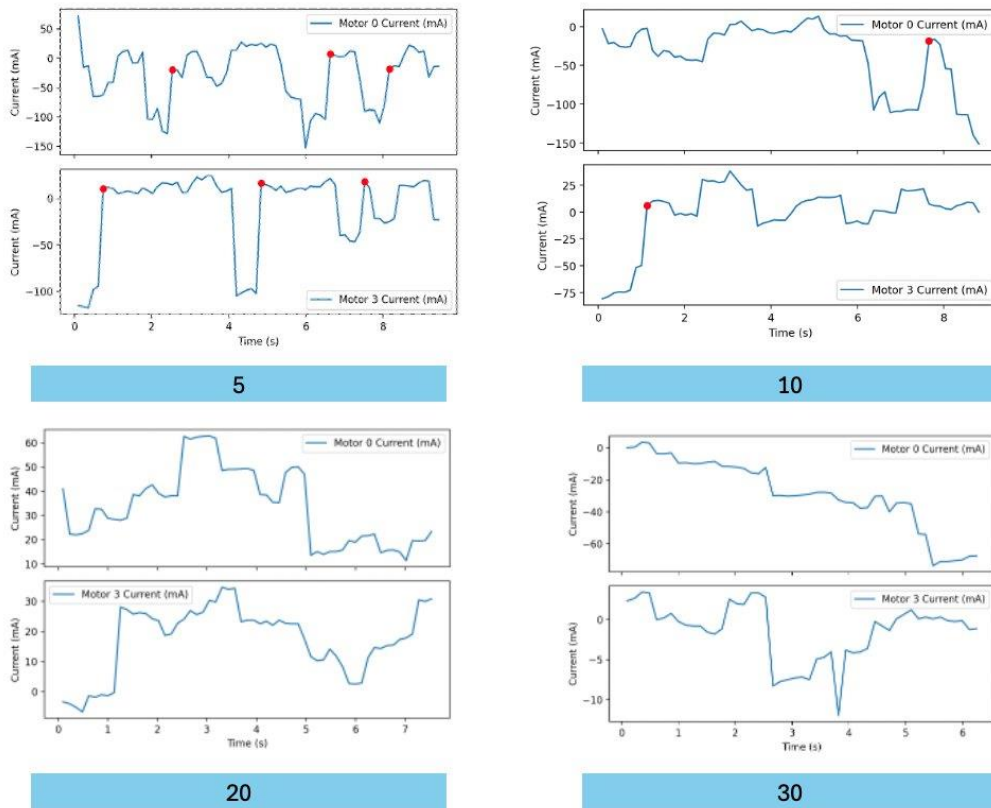


Figure 4. 11. Current feedback after applying moving average filter of various window sizes: 5, 10, 20, 30

After experimenting with various window sizes, a window size of 8 was most effective at maintaining a balance between noise reduction and significant data feature retention.

Moving average filter, however, introduces a delay in the signal as it takes time to compute the average of the specified window size. This delay becomes more pronounced with larger window sizes. As a result, the window size has to be limited to prevent it from affecting the real-time performance. The chosen window size of 8 minimizes this delay while still effectively smoothing the data as demonstrated in figure 4. 12.

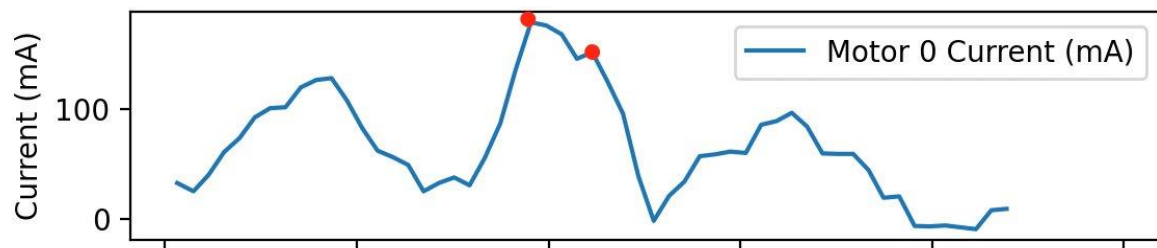


Figure 4. 12 Current feedback after applying the moving average filter of size 8

Additionally, this delay must be considered when calculating the home position. The system must account for the lag introduced by the filter to ensure the accuracy and precision of the home position tuning algorithm.

4.2.3 Peak Detection Algorithm

The peak detection algorithm is designed to identify the local maxima from the smoothed current feedback data. These points correspond to when the motor encounters resistance, indicating that the pulley's tip touched the wall. The flow of the peak detection algorithm is as follows:

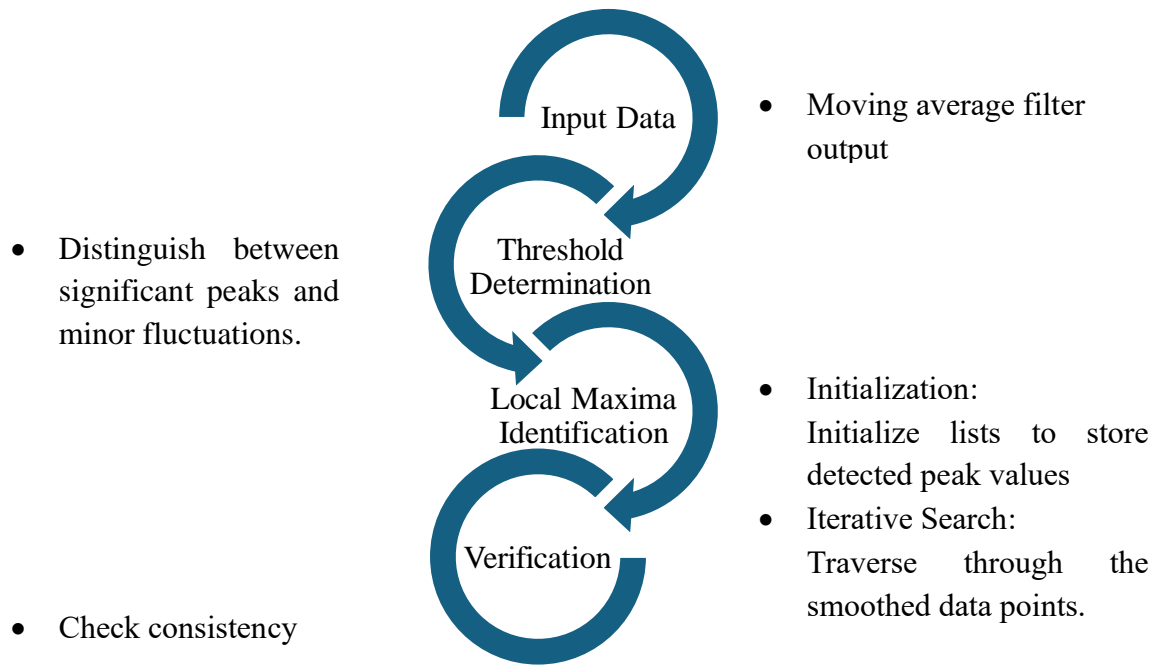


Figure 4. 13 Peak detection algorithm flowchart

In the current-based position control Mode, the motor controls the torque output by applying variable current values to reach a position setpoint. Real-time current feedback allows the motor to detect changes in load conditions. The objective of the following calculation is to determine appropriate current thresholds that can detect when the pulley tip is in contact with channel walls, for a range of sheath configurations of straight, $\sin(\frac{1}{2}x)$, $\sin(x)$.

The delay caused by the moving average filter is amended during peak detection. The algorithm adjusts the identified peak positions to compensate for the delay, ensuring that the detected peaks accurately represent the contact moments in real-time.

For setting current thresholds for current detection, the following steps are carried out:

1. Measure Baseline Current, $I_{baseline}$

The steady-state current of the motor, without any contact with the wall.

Configuration	$I_{baseline}$ (A)
Straight	0.5
$\sin (0.5x)$	0.7
$\sin (x)$	0.8

2. Measure Contact Current, $I_{contact}$

The current of the motor when the pulley tip contacts the wall

Configuration	$I_{contact}$ (A)
Straight	1.2
$\sin (0.5x)$	1.5
$\sin (x)$	1.8

3. Calculate Current Thresholds, $I_{threshold}$

$$\Delta I = I_{contact} - I_{baseline}$$

$$I_{threshold} = I_{baseline} + (\Delta I \times 0.7)$$

- Straight Configuration:

$$\Delta I = 1.2 - 0.5 = 0.7 \text{ A}$$

$$I_{threshold} = 0.5 + (0.7 \times 0.7) = 0.99 \text{ A}$$

- $\sin (\frac{1}{2}x)$ Configuration

$$\Delta I = 1.5 - 0.7 = 0.8 \text{ A}$$

$$I_{threshold} = 0.7 + (0.8 \times 0.7) = 1.26 \text{ A}$$

- $\sin (x)$ Configuration

$$\Delta I = 1.8 - 0.8 = 1.0 \text{ A}$$

$$I_{threshold} = 1.0 + (1.0 \times 0.7) = 1.7 \text{ A}$$

Using this information, the current limits are programmed within the motor controller to ensure that the system operates properly and within safety limits. The controller is programmed to measure the current, $I_{measured}$, of the motor. Within the control algorithm,

logic is provided to detect when $I_{contact}$ is greater than or equal to the threshold set current $I_{threshold}$. This condition shows that the pulley tip has contacted the wall of the endoscope's channel. The occurrence of this event will lead the control algorithm to the proper response, which involves stopping the movement of the motor and saving the position where the contact occurred.

Next, an extra check is performed against the motor performance graph to ensure the system operates safely. It should be verified that all the measured contact current values, $I_{contact}$ are within the continuous operating region, preventing overheating or damaging the motor. For example, if the limit for the motor's current operation is 2.0 A, then all $I_{contact}$ values shall be under this limit. This verifies that the operation is safe and is within the performance specification given by the motor.

4.2.4 Mapping of Motor Current to Torque

The relation between the motor current and output torque is necessary for predicting the motor's behavior in different load conditions. The torque that the motor can produce is given by the following equation:

$$T = K_t \times (I_{measured} - I_0)$$

$T = \text{motor output torque, Nm}$

$K_t = \text{motor torque constant, } \frac{Nm}{A}$

$I_{measured} = \text{measured motor current, A}$

$I_0 = \text{no-load motor current, A}$

The motor torque constant, K_t , is calculated using the stall torque, T_{stall} , and the stall current, I_{stall} , obtained through the manufacturer's specification:

$$T_{stall} = 8.4 \text{ Nm}, \quad I_{stall} = 6.6 \text{ A}$$

$$K_t = \frac{T_{stall}}{I_{stall}} = \frac{8.4 \text{ Nm}}{6.6 \text{ A}} = 1.27 \frac{\text{Nm}}{\text{A}}$$

Using the torque constant, the baseline torque and the contact torque are then calculated:

$$T_{baseline} = K_t \times (I_{baseline} - I_0) = \frac{1.27 \text{ Nm}}{\text{A}} \times (0.5 \text{ A} - 0.4 \text{ A}) = 0.127 \text{ Nm}$$

$$T_{contact} = K_t \times (I_{contact} - I_0) = \frac{1.27 \text{ Nm}}{\text{A}} \times (1.2 \text{ A} - 0.4 \text{ A}) = 1.016 \text{ Nm}$$

4.2.5 Home Positioning Control Algorithm Development

The final step in the software implementation is to calculate the home position of the pulley's tip within the walls. The home position is determined by identifying the midpoint between the corresponding angles of two current peaks. The following steps are carried out to facilitate a smooth and efficient calculation of the home position:

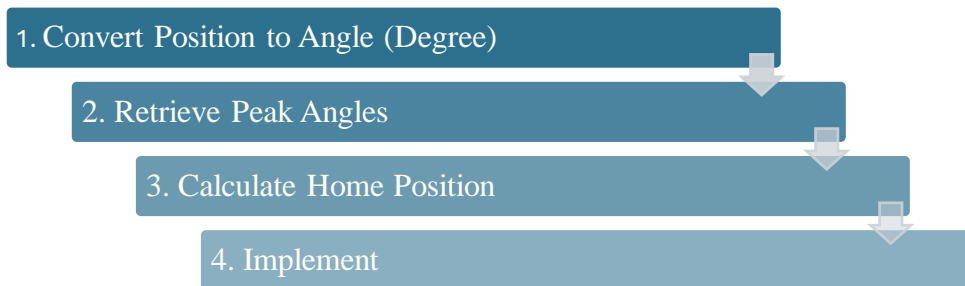


Figure 4. 14 Home position calculation procedures flowchart

1. **Convert Position to Degree:** Current readings from the Dynamixel-106 motor are converted to angular positions. The motor's position values, given in steps, are translated into degrees to understand the physical angular position of the pulley or robotic gripper.

- Position feedback: 4096 steps for 360°
- Formula:

$$\theta = \frac{\text{position}}{4096} \times 360$$

$$\theta = \text{angular position in degrees}$$

$$\text{position} = \text{motor position value in steps, ranging from 0 to 4095}$$

2. **Retrieve Peak Angles:**

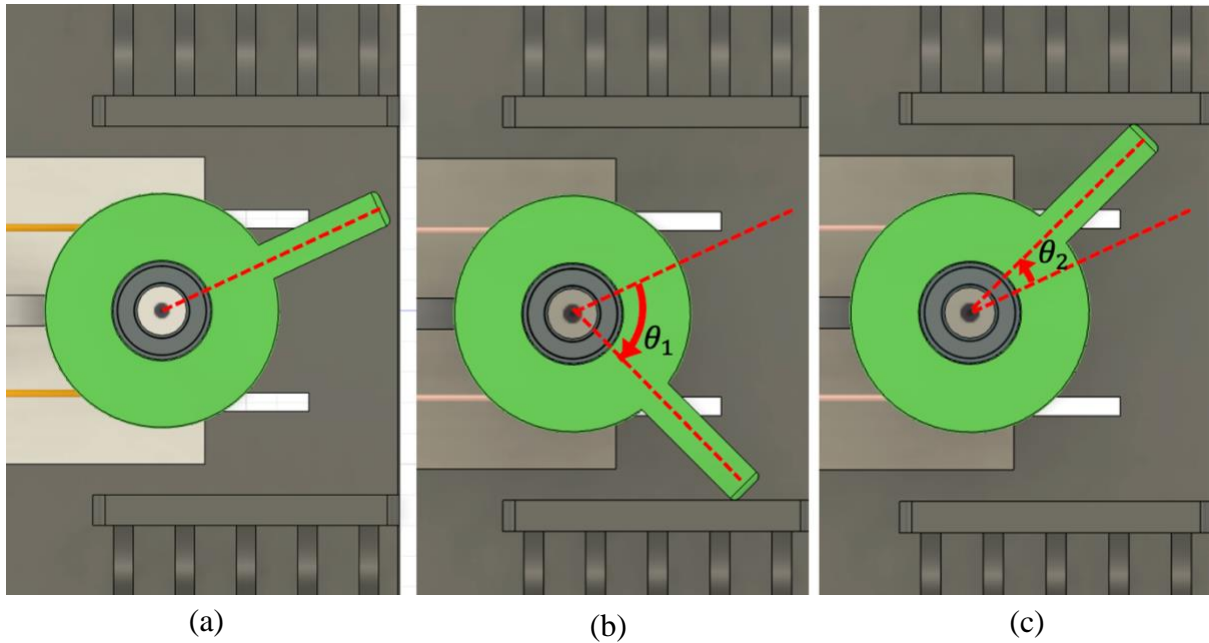


Figure 4. 15 (a) Initial Position (b) First peak angle – touches the right wall (c) second peak angle – touches the left wall

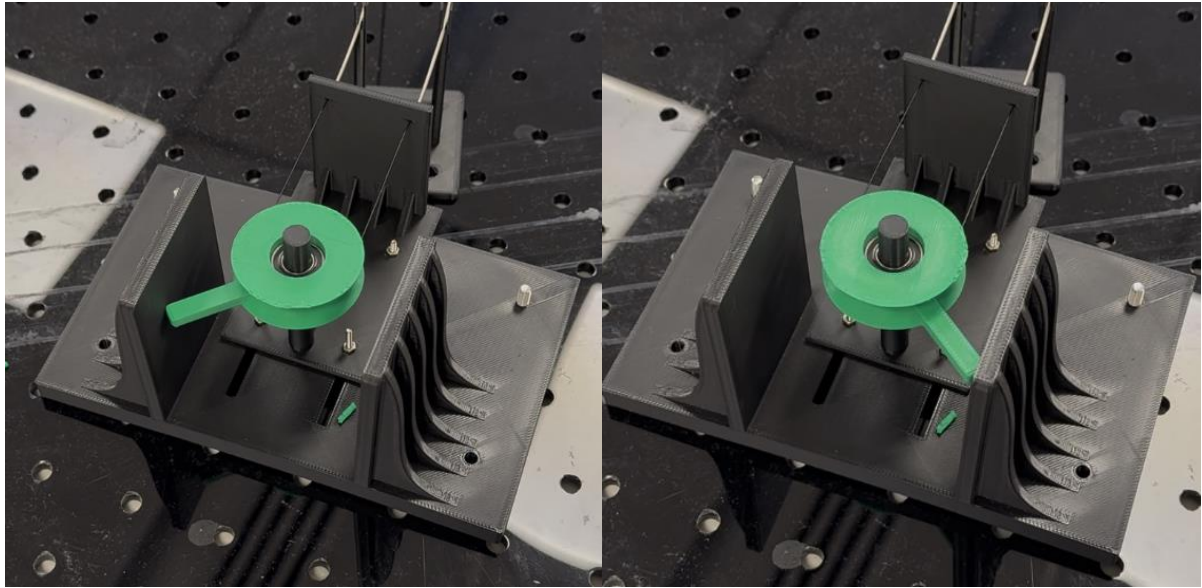


Figure 4. 16 3D-printed distal pulley touching the right and left wall

- Angles represent the position of the pulley's tip.
- When the pulley's tip touches the walls, there will be peaks in the current feedback graph.

3. Calculate Midpoint:

- The home position is calculated by taking the average of the two peak angles.
- Formula:

$$\theta_{home} = \frac{(\theta_1 + \theta_2)}{2}$$

θ_1 = angle at the first peak

θ_2 = angle at the second peak

4. **Implementation:**

- The calculated home position is stored and used as a reference for the pulley's neutral position within the walls.
- For validation, several measurements of θ_1 and θ_2 are taken in order to account for any inconsistencies or errors. The algorithm computes the average of the different sets of measurements to achieve an improved estimation with a reduction of outliers.
- The algorithm is capable of handling anomalies, such as missed current peaks and inconsistent readings. When error is detected, it implements timeout mechanisms and repeat the measure if required.
- The same algorithmic approach can be followed to calibrate the home position of a robotic gripper inside an endoscope channel. The control system will provide a reliable home position by detecting the contact points of the gripper's movement limits and calculating the midpoint, which enhances the safety and effectiveness of the endoscopic robotic operation.

5. RESULTS AND DISCUSSION

5.1 Results

θ_{home} is calculated with end pulley's initial position as a reference point. As algorithm is tested with random initial positions, the collected home position angle will be trial-specific, making it difficult to compare data. To resolve this issue, θ_{err} is calculated and used for measuring the performance of the control algorithm:

$$\theta_{err} = \theta_{experimental\ home\ position} - \theta_{theoretical\ home\ position}$$

Table 1: Compiled Data of θ_{err}

Straight, θ_{err}			
	Smallest	Middle	Largest
Trial 1	2.75°	1.45°	0.1°
Trial 2	3.24°	2.16°	0.14°
Trial 3	3.01°	4.07°	1.5°
Trial 4	2.73°	1.45°	0.1°
Trial 5	3.27°	2.13°	0.14°
Trial 6	3.01°	4.1°	1.5°
Sin(0.5x), θ_{err}			
	Smallest	Middle	Largest
Trial 1	2.2°	1.45°	0.85°
Trial 2	5.68°	2.16°	0.97°
Trial 3	4.51°	6.07°	1.06°
Trial 4	2.3°	1.46°	1.84°
Trial 5	5.59°	2.16°	0.97°
Trial 6	4.51°	6.06°	0.06°
Sin(x), θ_{err}			
	Smallest	Middle	Largest
Trial 1	0.93°	1.89°	1.06°
Trial 2	2.16°	2.33°	1.23°
Trial 3	7.7°	3.56°	1.11°
Trial 4	0.93°	2.09°	1.05°
Trial 5	2.16°	2.33°	1.24°
Trial 6	7.7°	3.36°	1.11°

5.1.1 Straight Configuration

5.1.1.1 Straight, Smallest Angle – 52.7°

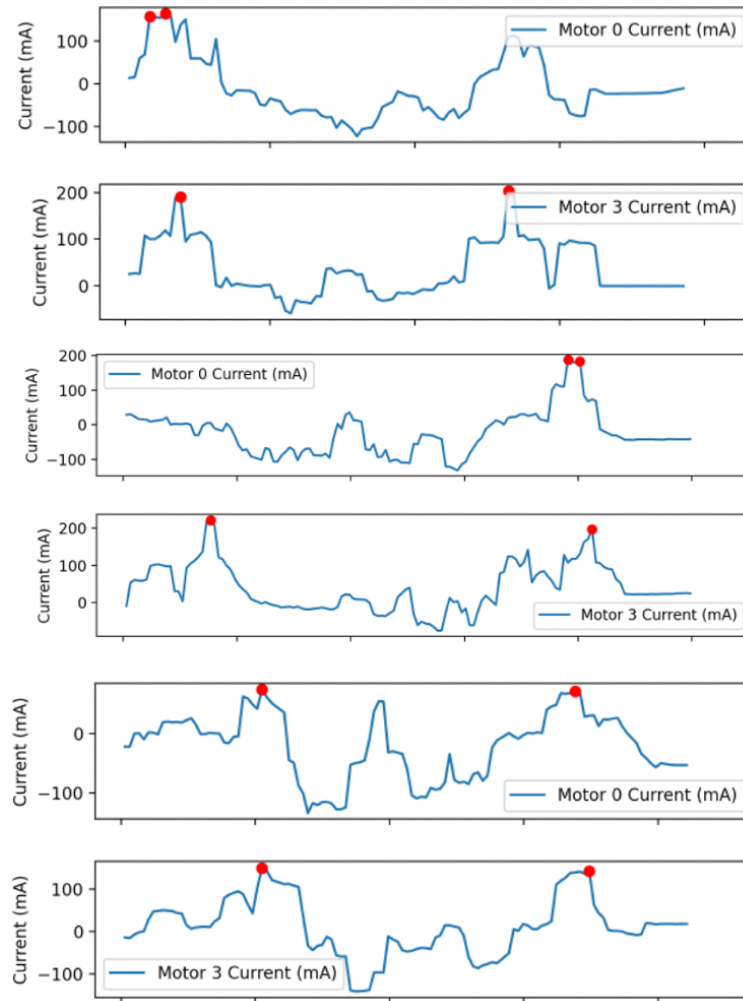


Figure 5.1 Straight, Smallest Angle – 52.7° Graph [Current vs Time]

Table 2: Average Error Computed in Straight, Smallest Angle – 52.7°

	Trial 1	Trial 2	Trial 3	Trial 4	Trial 5	Trial 6
θ_{err}	2.75°	3.24°	3.01°	2.73°	3.27°	3.01°
$\theta_{avg.err}$	3.00°					
σ	$\sigma = \sqrt{\sum \frac{(x_i - \mu)^2}{N}} = 0.23^\circ$					

5.1.1.2 Straight, Middle Angle – 53.3°

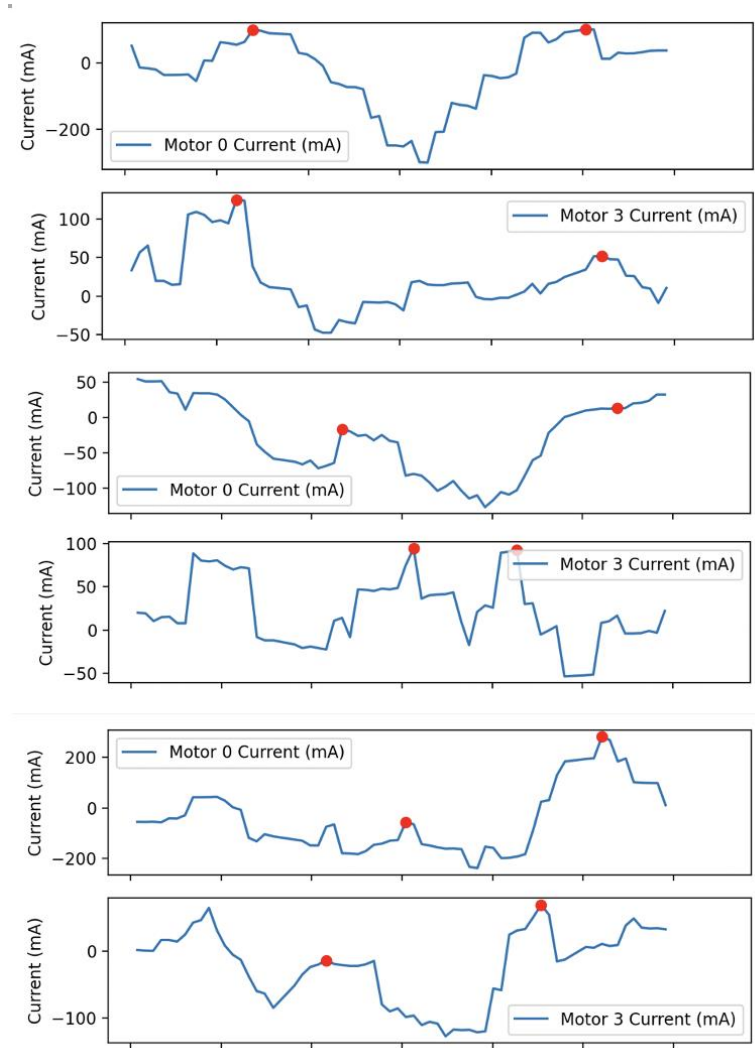


Figure 5.2 Straight, Middle Angle – 53.3° Graph [Current vs Time]

Table 3: Average Error Computed in Straight, Middle Angle – 53.3

	Trial 1	Trial 2	Trial 3	Trial 4	Trial 5	Trial 6
θ_{err}	1.45°	2.16°	4.07°	1.45°	2.13°	4.1°
$\theta_{avg.err}$	2.56°					
σ	$\sigma = \sqrt{\sum \frac{(x_i - \mu)^2}{N}} = 1.22^\circ$					

5.1.1.3 Straight, Largest Angle – 53.9°

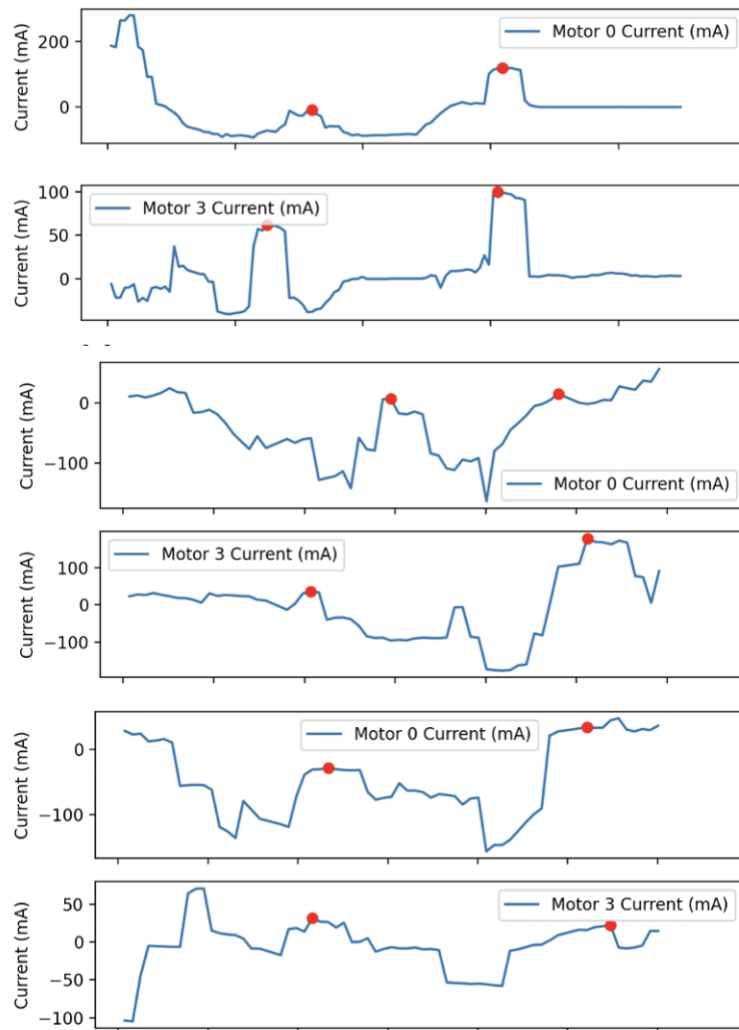


Figure 5. 3 Straight, Largest Angle – 53.9° Graph [Current vs Time]

Table 4: Average Error Computed in Straight, Largest Angle – 53.9°

	Trial 1	Trial 2	Trial 3	Trial 4	Trial 5	Trial 6
θ_{err}	0.1°	0.14°	1.5°	0.1°	0.14°	1.5°
$\theta_{avg.err}$	0.58°					
σ	$\sigma = \sqrt{\sum \frac{(x_i - \mu)^2}{N}} = 0.71^\circ$					

5.1.2 Curved Configuration, $\sin(0.5x)$,

5.1.2.1 $\sin(\frac{1}{2}x)$, Smallest Angle – 52.7°

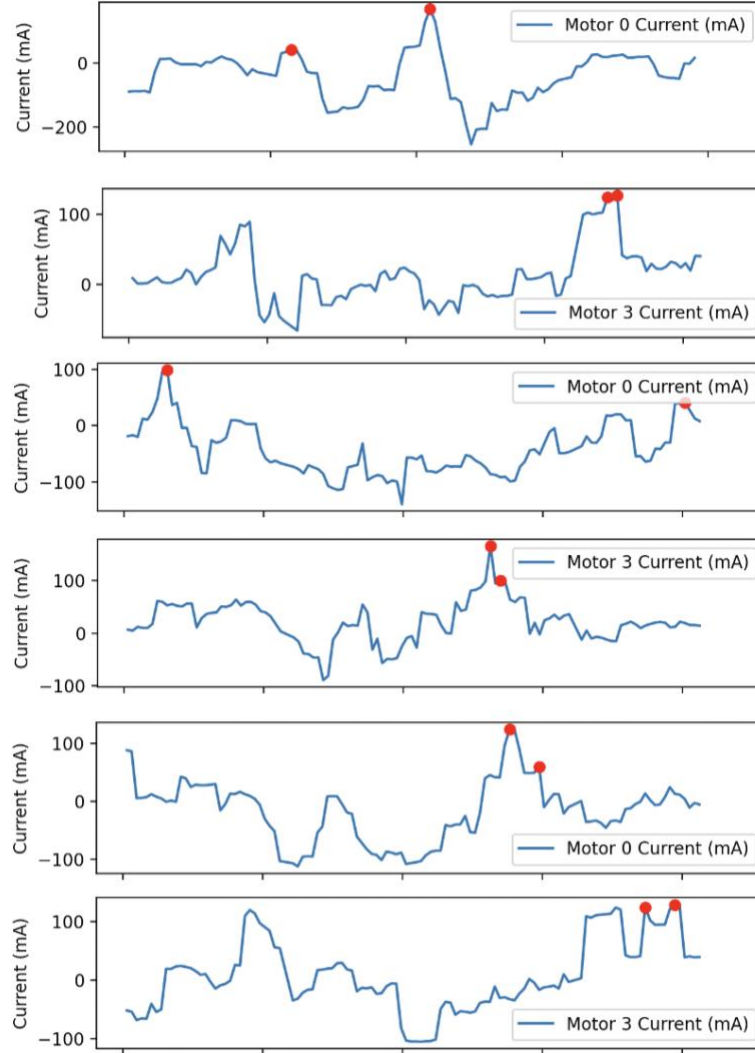


Figure 5. 4 $\sin(0.5x)$, Smallest Angle, 52.7° [Current vs Time]

Table 5: Average Error Computed in $\sin(0.5x)$, Smallest Angle – 52.7°

	Trial 1	Trial 2	Trial 3	Trial 4	Trial 5	Trial 6
θ_{err}	2.2°	5.68°	4.51°	2.3°	5.59°	4.51°
$\theta_{avg.err}$	4.13°					
σ	$\sigma = \sqrt{\sum \frac{(x_i - \mu)^2}{N}} = 1.54^\circ$					

5.1.2.2 $\sin(\frac{1}{2}x)$, Middle Angle – 53.3°

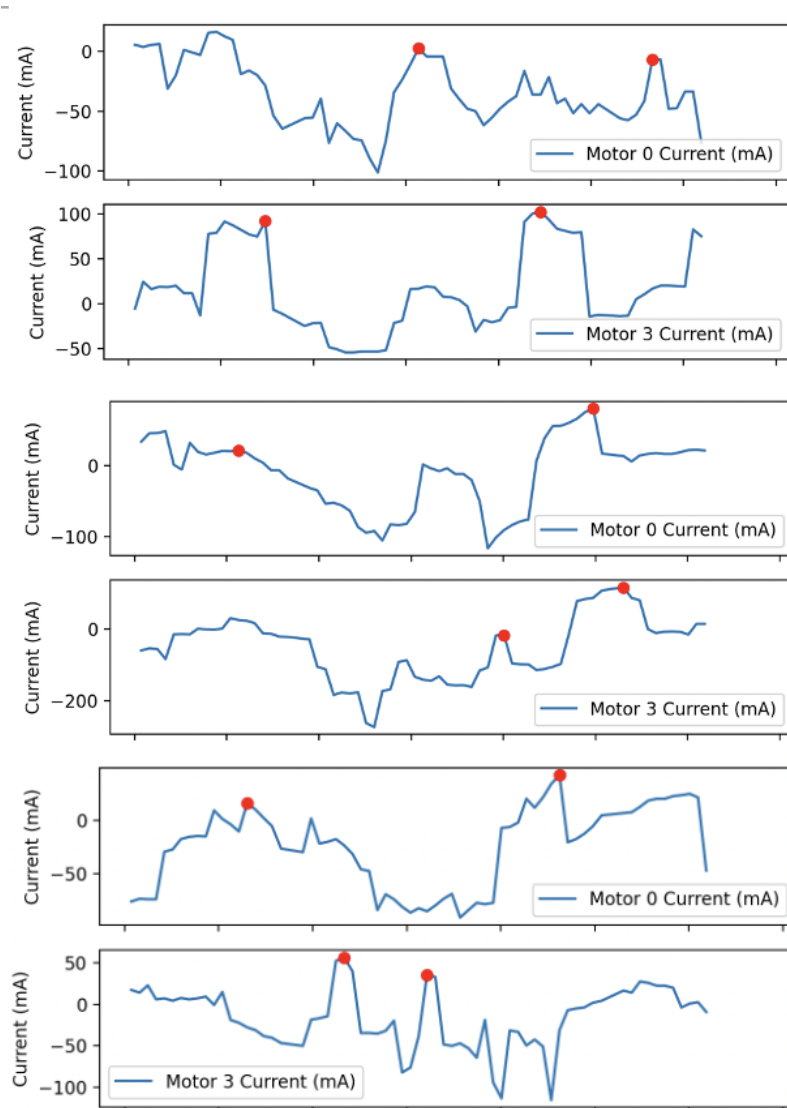


Figure 5. $5 \sin(0.5x)$, Middle Angle, 53.3° [Current vs Time]

Table 6: Average Error Computed in $\sin(0.5x)$, Middle Angle – 53.3°

	Trial 1	Trial 2	Trial 3	Trial 4	Trial 5	Trial 6
θ_{err}	1.45°	2.16°	6.07°	1.46°	2.16°	6.06°
$\theta_{avg.err}$	3.23°					
σ	$\sigma = \sqrt{\sum \frac{(x_i - \mu)^2}{N}} = 2.22^\circ$					

5.1.2.3 $\sin(\frac{1}{2}x)$, Largest Angle – 53.9°

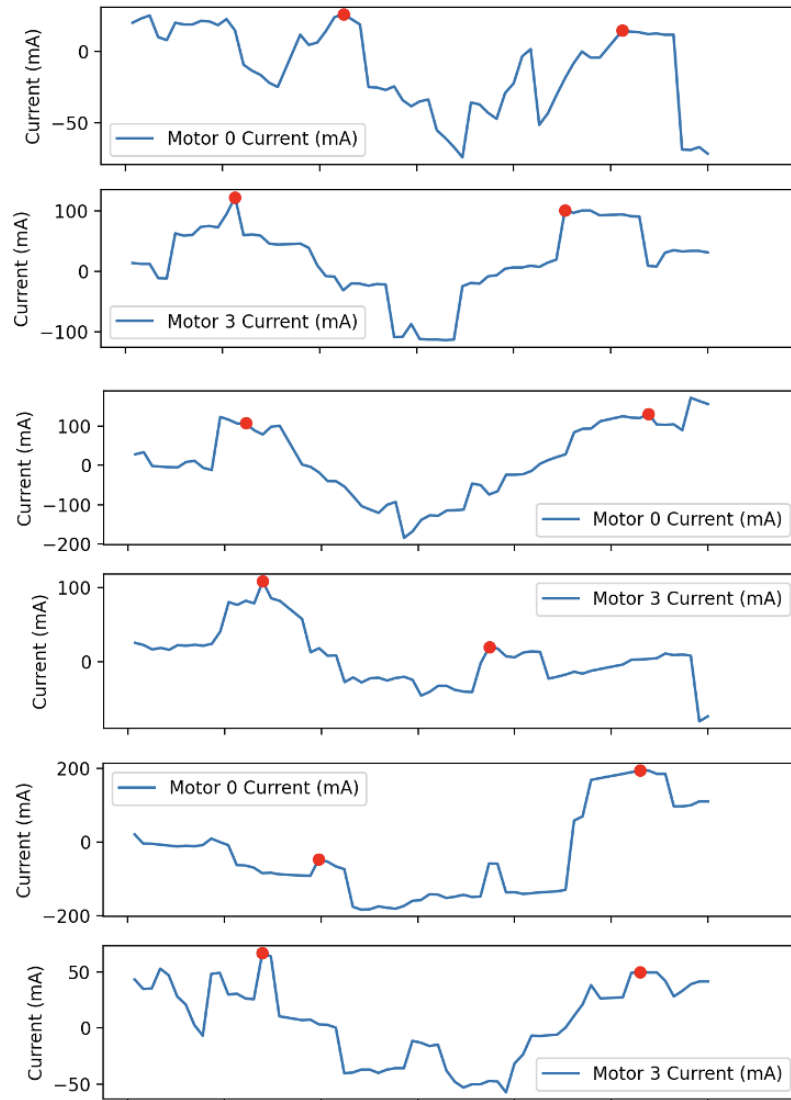


Figure 5.6 $\sin(0.5x)$, Largest Angle, 53.9° [Current vs Time]

Table 7: Average Error Computed in $\sin(0.5x)$, Largest Angle – 53.9°

	Trial 1	Trial 2	Trial 3	Trial 4	Trial 5	Trial 6
θ_{err}	0.85°	0.97°	1.06°	1.84°	0.97°	0.06°
$\theta_{avg.err}$	0.96°					
σ	$\sigma = \sqrt{\sum \frac{(x_i - \mu)^2}{N}} = 0.57^\circ$					

5.1.3 Curved Configuration, Sin(x)

5.1.3.1 Sin(x), Smallest Angle – 52.7°

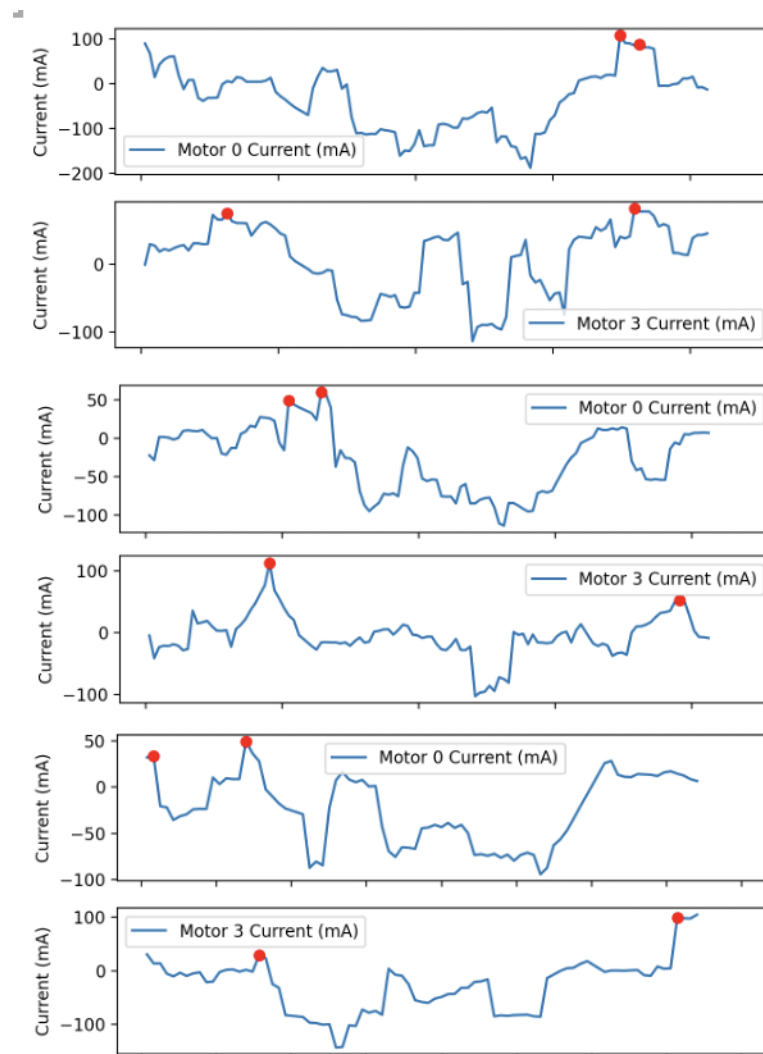


Figure 5. 7 Sin(x), Smallest Angle, 52.7° [Current vs Time]

Table 8: Average Error Computed in sin(x), Smallest Angle – 52.7°

	Trial 1	Trial 2	Trial 3	Trial 4	Trial 5	Trial 6
θ_{err}	0.93°	2.16°	7.7°	0.93°	2.16°	7.7°
$\theta_{avg.err}$	3.6°					
σ	$\sigma = \sqrt{\sum \frac{(x_i - \mu)^2}{N}} = 3.23^\circ$					

5.1.3.2 Sin(x), Middle Angle – 53.3°

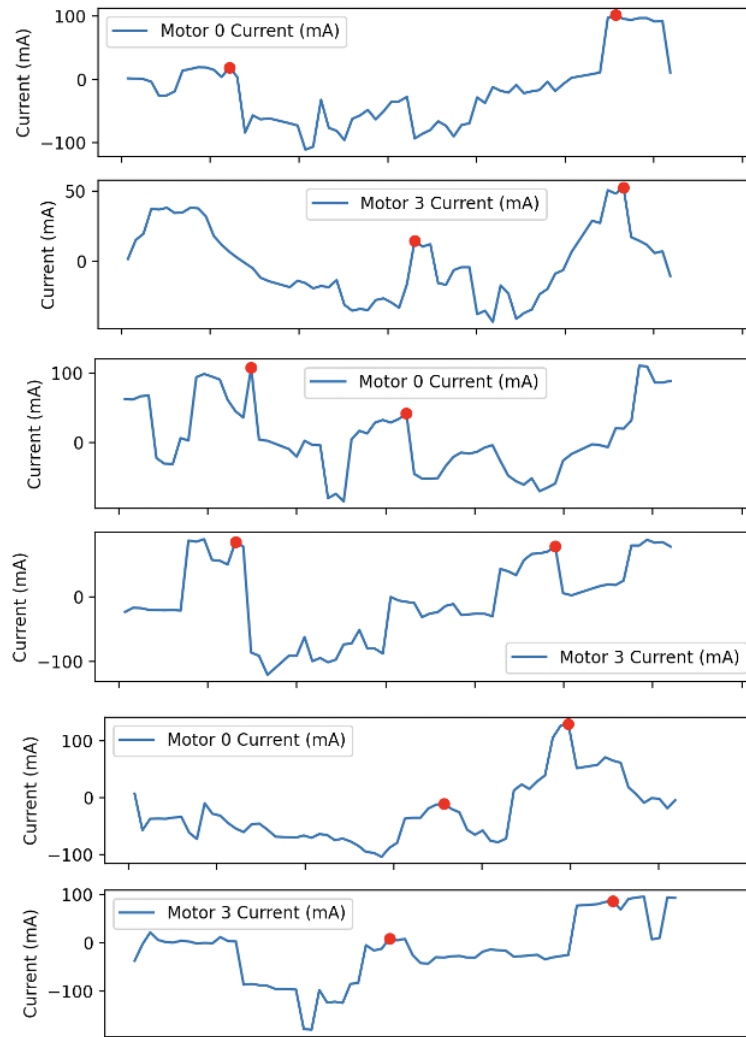


Figure 5. 8 Sin(x), Middle Angle, 53.3° [Current vs Time]

Table 9: Average Error Computed in sin(x), Middle Angle – 53.3°

	Trial 1	Trial 2	Trial 3	Trial 4	Trial 5	Trial 6
θ_{err}	1.89°	2.33°	3.56°	2.09°	2.33°	3.36°
$\theta_{avg.err}$	2.6°					
σ	$\sigma = \sqrt{\sum \frac{(x_i - \mu)^2}{N}} = 0.96^\circ$					

5.1.3.3 Sin(x), Largest Angle – 53.9°

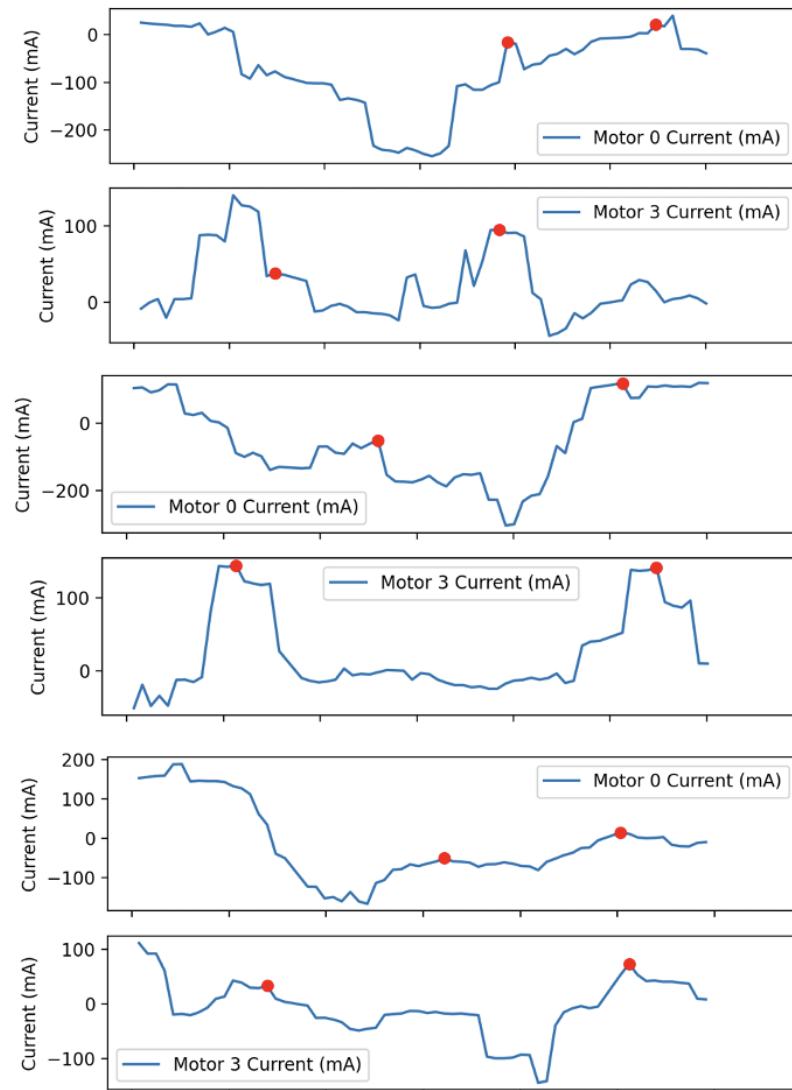


Figure 5. 9 Sin(x), Largest Angle, 53.9° [Current vs Time]

Table 10: Average Error Computed in sin(x), Largest Angle – 53.9°

	Trial 1	Trial 2	Trial 3	Trial 4	Trial 5	Trial 6
θ_{err}	1.06°	1.23°	1.11°	1.05°	1.24°	1.11°
$\theta_{avg.err}$	1.14°					
σ	$\sigma = \sqrt{\sum \frac{(x_i - \mu)^2}{N}} = 0.08^\circ$					

5.2 Discussion

5.2.1 Performance of the Control Algorithm

The control algorithm automated home position calibration for a total of 9 sheath configurations of different curvatures and contact angles. Trials were conducted with different initial starting points, resulting in different home position values. The algorithm's accuracy was measured by computing the error, the difference between the theoretical value and experimental value.

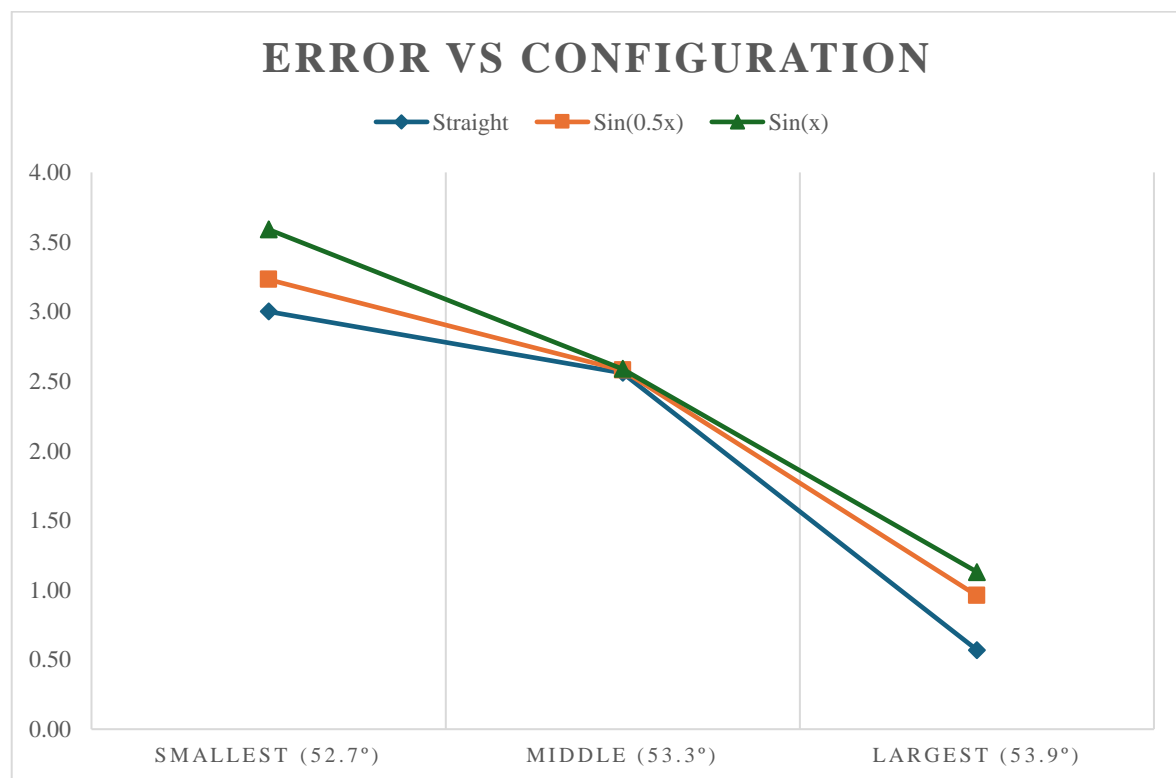


Figure 5. 10 Graph of Error, Configuration, and Contact Angle

The control algorithm displays varied levels of accuracy across different sheath configurations, as supported by the error values across the trials. Overall, the algorithm's performance was considerably accurate, with certain configurations yielding higher accuracy. Notably, the sheath with a straight configuration, particularly at the largest contact angle, resulted in the lowest average error (0.57), indicating that this combination was closest to the

theoretical value. This suggests that in simpler configurations (i.e., minimal curvature and larger contact angles), the algorithm calibrates the home position with minimal error. However, for more complex configurations, especially involving higher curvature and smaller contact angles, the algorithm exhibited higher errors, suggesting areas for potential refinement.

5.2.2 Impact of Sheath Curvature and Contact Angle on Algorithm Performance

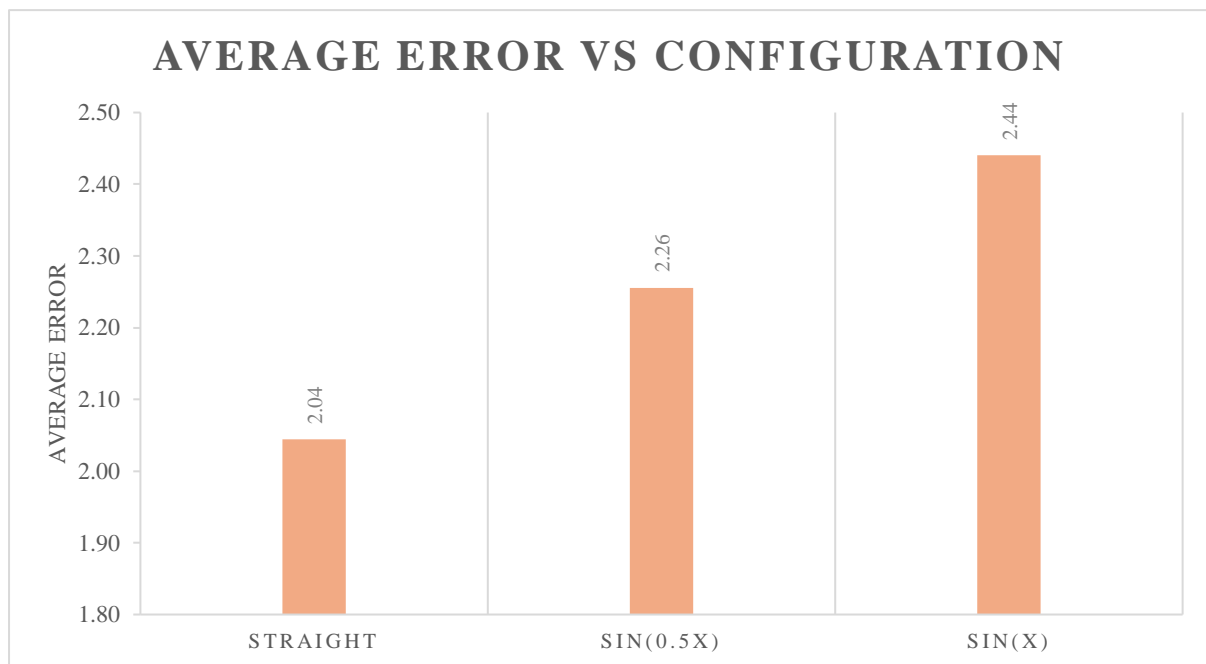


Figure 5. 11 Graph of Average Error vs Configuration

The algorithm's performance was significantly affected by the curvature of the sheath. Three distinct curvature types were tested: Straight, Sin(0.5x), and Sin(x). As demonstrated in Figure 5.11, the straight configuration consistently showed lower average error values across different contact angles, indicating that the control algorithm performs more accurately when curvature is minimized. In contrast, the "Sin(x)" configuration, which introduces the highest curvature, yielded higher average error values, particularly noticeable in the largest contact angle scenario, where the error peaked at 3.59. This pattern suggests that as curvature increases,

the control algorithm may struggle to maintain accuracy, potentially due to increased complexity in the robot's mechanical adjustments to match the theoretical home position.

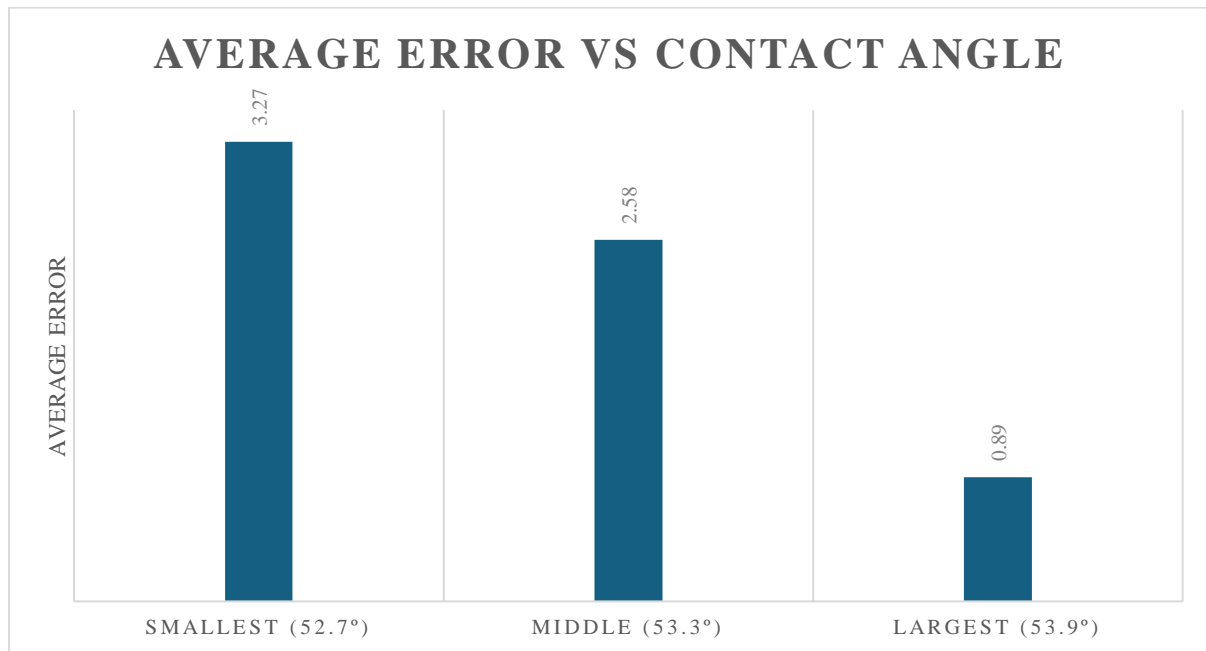


Figure 5. 12 Graph of Average Error vs Contact Angle

Contact angle also played a critical role in the algorithm's accuracy. The smallest contact angle, 52.7° , was generally associated with higher errors, especially in the $\sin(x)$ and $\sin(0.5x)$ curvature configurations. This trend suggests that smaller contact angles may add to the complexity of the calibration process, potentially due to the constraints they impose on the robot's alignment and movement. In contrast, the largest contact angle, 53.9° , tended to produce lower average errors across all curvature types. This pattern indicates that larger contact angles allow the algorithm greater flexibility in calibrating to the theoretical home position, eventually enhancing the accuracy. Overall, the impact of contact angle was particularly notable in high-curvature scenarios, where larger contact angles seemed to mitigate the calibration difficulty associated with curvature.

5.2.3 Underlying Factors Influencing Calibration Accuracy

The control algorithm's accuracy in achieving the home position is notably influenced by both sheath curvature and contact angle, as reflected in the error values across different configurations. The result suggests a strong interplay between these two factors, where certain combinations are more challenging for the algorithm to handle accurately.

- Path Complexity and Positional Precision in High Curvature:

High curvature, such as $\sin(x)$, introduces non-linear paths that require the tool to perform complex adjustments. The algorithm must execute finer, more precise movements to align with the theoretical home position, which increases the chance of cumulative error. These calibration challenges become more prominent when paired with smaller contact angles, where the tool's range of movement is limited, compounding alignment difficulties.

- Spatial Constraints with Smaller Contact Angles:

The smallest contact angle, 52.7° , configuration provides less room for positional adjustments, intensifying calibration difficulty. This limited range magnifies minor misalignments, as the tool lacks the freedom to make fine corrections. Also, with high curvatures, the combined constraints of non-linear paths and restricted movement range exacerbate error accumulation.

- Increased Frictional Resistance in Tight Configurations:

Smaller contact angles, particularly in curved sheaths, may subject the tool to increased lateral force within the sheath, leading to higher friction and resistance. This mechanical resistance hinders smooth calibration adjustments and can cause misalignment, especially under high-curvature conditions. The frictional forces further

challenge the algorithm's ability to position the tool precisely, increasing the likelihood of calibration errors.

- Enhanced Flexibility and Buffering Effect of Larger Angles:

Larger contact angles provide greater spatial freedom, allowing the tool to make necessary positional adjustments with minimal resistance. This flexibility acts as a buffer against small misalignments, enabling the algorithm to achieve more accurate home position calibration. When combined with lower curvature, it minimizes both path complexity and mechanical constraints, leading to the most accurate results.

5.2.4 Advantages of Using Motor Current Readings

Using motor current readings for home position tuning offers few key advantages. First, motor currents give instantaneous feedback of torque and resistance the system is under, and hence it can be adjusted immediately. This instantaneous feedback enhances the responsiveness of the system, making it easier to maintain accurate positioning. Next, relying on motor current feedback eliminates the need for additional sensors, minimizing the complexity of system hardware and reducing potential points of failure. Moreover, the algorithm's ability to perform automatic home position calibration lowers the likelihood of human error, streamlining the calibration process and improving overall reliability.

5.2.5 Limitations

While the control algorithm demonstrated effectiveness in achieving the home position across various sheath curvatures and contact angles, several limitations emerged that impacted its accuracy and consistency. One primary limitation is the lack of compensatory mechanisms

for nonlinearities inherent in the tendon-sheath system, such as friction, hysteresis, and backlash. Without modelling these factors, the algorithm is unable to fully adjust for the variations, especially in configurations with high curvatures and varying contact angles. The algorithm's reliance on simple averaging assumes a linear and symmetric response, which does not hold true in these conditions. This assumption likely contributes to the accumulated error variability.

While the algorithm achieves high calibration accuracy in low-curvature, large-angle configurations, real surgical scenarios often involve high curvature and varying contact angles. These more complex conditions demand precise control, which the current algorithm struggles to provide without modeling the nonlinearities inherent in such scenarios.

To address these limitations, future improvements could incorporate adaptive control strategies that account for friction, hysteresis, and backlash. Such enhancements would improve calibration accuracy across a broader range of sheath configurations, aligning the algorithm's performance with the demands of realistic surgical applications.

6. FUTURE WORKS

The design of the control algorithm based on motor current has held promise for automation in home position calibration for endoscopic surgical robots. However, there are various future directions that the idea can be improved and expanded upon.

Firstly, the control algorithm could be refined by integrating sophisticated models for friction, hysteresis, and backlash. Proper modeling of these mechanical nonlinearities allows their influence to be compensated for. This would make the algorithm more robust against higher sheath curvature or changes in operating conditions. The realization of active control methods that change their parameter settings based on feedback may further increase the robustness and responsiveness of the algorithm.

Secondly, hardware can be further optimized by fine-tuning the mechanical parts of the system. Applying bearings with a low friction coefficient or using materials of superior mechanical properties will reduce unwanted resistive forces and variability within the system. Research into other various gripper designs or tendon materials may also yield better responsiveness and reliability for the system.

Thirdly, extended testing and validation will confirm and point out limitations under diverse conditions. The testing for various sheath lengths, with higher degree curvatures, and in simulated anatomical environments will provide grounds to assess the algorithm's practical applicability. Tests performed by a medical professional where the system is presented with realistic scenarios will be helpful.

Finally, the concept of motor current readings for automated calibration and contact detection can be applied well beyond endoscopic surgical robots. Industrial robotics will leap with the enhanced accuracy and productivity of robotic arms working on assembly lines or performing material handling through automation of joint position calibrations and surface

contact detection without additional sensors. Also, in prosthetics and exoskeletons, embedding motor current-based control algorithms will make the assistive device more responsive and self-adapting. Since the motor current provides a view into how the user interacts with the environment or their self-movement, it allows for an intuitive approach toward control with fewer complex arrays of sensors.

This will be very helpful for remote-operated vehicles and, in general, drones performing tasks with physical interaction, like underwater exploration or environmental monitoring, by enabling it to detect obstacles or surface contact using only motor current feedback. This enhances safety and effectiveness during operations without extra hardware which is not practical in such an environment.

7. CONCLUSION

This research successfully demonstrated the feasibility of using motor current reading to calibrate the robotic gripper to the home position in endoscopic surgical robots. When the control algorithm is implemented in a real surgical scenario, it can detect contact points between the robotic gripper and channel walls of the endoscope, while calculating the home position precisely within different sheath configurations. Dynamic adjustment of current thresholds allows changes in friction and resistance due to sheath curvature to be accommodated by the algorithm, furthering its robustness and reliability.

Using motor current readings addresses an important gap in current methodologies by eliminating the need for manual adjustments or any other sensors, thereby enhancing efficiency and safety in robotic endoscopic procedures. Moreover, the concept's applicability extends beyond surgical robots, with its potential use in industrial automation, prosthetics, and remote-operated vehicles. The approach is cost-effective and efficient as it can be integrated with an existing motor feedback system. However, to achieve this, further improvements are required for a higher level of precision and adaptability. This can be obtained by incorporating the models of mechanical nonlinearities and implementing adaptive control strategies.

In conclusion, the current-based motor control algorithm presents a promising approach to surgical robotics. It opens paths to further developments for obtaining more precise, reliable, and efficient robotic systems in various fields. Additional research in this direction promises great technological advances that will serve a wide circle of applications and branches of industry.

8. REFERENCES

- [1] C. Staub, K. Ono, H. Mayer, A. Knoll, H. Ulbrich, and R. Bauernschmitt, "Remote Minimally Invasive Surgery – Haptic Feedback and Selective Automation in Medical Robotics," *Applied Bionics and Biomechanics*, vol. 8, no. 2, p. 765172, 2011, doi: 10.3233/ABB-2011-0022.
- [2] C. Vaida et al., "Robotics in minimally invasive procedures: History, current trends and future challenges," 6th International Conference on Advancements of Medicine and Health Care through Technology; 17–20 October 2018, Cluj-Napoca, Romania, pp. 267–273, 2019. doi:10.1007/978-981-13-6207-1_41
- [3] O. Wyman and O. Eitelwein, "Positioning the industry for growth in robotic surgery," Oliver Wyman - Impact-Driven Strategy Advisors, <https://www.oliverwyman.com/our-expertise/perspectives/health/2023/august/positioning-the-industry-for-growth-in-robotic-surgery.html> (accessed Aug. 15, 2024).
- [4] H. Yeganeh, "An analysis of emerging trends and transformations in Global Healthcare," *International Journal of Health Governance*, vol. 24, no. 2, pp. 169–180, May 2019. doi:10.1108/ijhg-02-2019-0012
- [5] C. M. Oliveira et al., "Robotic surgery in otolaryngology and head and Neck Surgery: A Review," *Minimally Invasive Surgery*, vol. 2012, pp. 1–11, 2012. doi:10.1155/2012/286563
- [6] B. Cheon, H. Baek, C. Kim, J. Ahn, and D. Kwon, "Intuitive master device for endoscopic robots with visual-motor correspondence," *The International Journal of Medical Robotics and Computer Assisted Surgery*, vol. 18, no. 3, Apr. 2022. doi:10.1002/rcs.2397
- [7] Z. Wang, Z. Sun, and S. J. Phee, "Modeling tendon-sheath mechanism with flexible configurations for Robot Control," *Robotica*, vol. 31, no. 7, pp. 1131–1142, May 2013. doi:10.1017/s0263574713000386
- [8] X. Li *et al.*, "Deep learning for haptic feedback of flexible endoscopic robot without prior knowledge on sheath configuration," *International Journal of Mechanical Sciences*, vol. 163, p. 105129, Nov. 2019. doi:10.1016/j.ijmecsci.2019.105129
- [9] M. Yin, Z. Xu, Z. Zhao, and H. Wu, "Mechanism and position tracking control of a robotic manipulator actuated by the tendon-sheath," *Journal of Intelligent & Robotic Systems*, vol. 100, no. 3–4, pp. 849–862, Aug. 2020. doi:10.1007/s10846-020-01245-6
- [10] Y. Li *et al.*, "Automatic Robot-world calibration in an optical-navigated surgical robot system and its application for oral implant placement," *International Journal of Computer Assisted Radiology and Surgery*, vol. 15, no. 10, pp. 1685–1692, Jul. 2020. doi:10.1007/s11548-020-02232-w

- [11] G. Tholey, A. Pillarisetti, W. Green, and J. P. Desai, "Design, development, and testing of an automated laparoscopic grasper with 3-D force measurement capability," *Lecture Notes in Computer Science*, pp. 38–48, Jun. 2004. doi:10.1007/978-3-540-25968-8_5
- [12] *Intuitive.com*, 2024. <https://www.intuitive.com/en-us/products-and-services/da-vinci/da-vinci-systems> (accessed Oct. 10, 2024).
- [13] A. Simorov, R. S. Otte, C. M. Kopietz, and D. Oleynikov, "Review of Surgical Robotics user interface: What is the best way to control robotic surgery?," *Surgical Endoscopy*, vol. 26, no. 8, pp. 2117–2125, Feb. 2012. doi:10.1007/s00464-012-2182-y
- [14] Jun Isogaki *et al.*, "Robot-Assisted Surgery for Gastric Cancer: Experience at Our Institute," *Pathobiology*, vol. 78, no. 6, pp. 328–333, Jan. 2011, doi: 10.1159/000330172.
- [15] A. Y. Lee *et al.*, "Da vinci robot-assisted endoscopic full-thickness gastric resection with regional lymph node dissection using a 3D near-infrared video system: A Single-Center 5-year clinical outcome," *Surgical Endoscopy*, vol. 38, no. 4, pp. 2124–2133, Mar. 2024. doi:10.1007/s00464-024-10722-0
- [16] R. Tsang, "Transoral robotic surgery: Development and challenges," *Robotic Surgery: Research and Reviews*, p. 1, Jan. 2015. doi:10.2147/rsrr.s50259
- [17] T. N. Do, T. Tjahjowidodo, M. W. Lau, and S. J. Phee, "Dynamic friction-based force feedback for tendon- sheath mechanism in notes system," *International Journal of Computer and Electrical Engineering*, vol. 6, no. 3, pp. 252–258, 2014. doi:10.7763/ijcee.2014.v6.833
- [18] S. V. Kantsevov *et al.*, "Transgastric endoscopic splenectomy," *Surgical Endoscopy and Other Interventional Techniques*, vol. 20, no. 3, pp. 522–525, Jan. 2006, doi: 10.1007/s00464-005-0263-x.
- [19] S. J. Phee *et al.*, "Master and slave transluminal endoscopic robot (MASTER) for natural orifice transluminal endoscopic surgery (NOTES)," 2009 Annual International Conference of the IEEE Engineering in Medicine and Biology Society, Sep. 2009. doi:10.1109/iembs.2009.5333413
- [20] G. Tay, H. Tan, T. K. Nguyen, S. J. Phee, and N. G. Iyer, "Use of the endomaster robot-assisted surgical system in transoral robotic surgery: A cadaveric study," *The International Journal of Medical Robotics and Computer Assisted Surgery*, vol. 14, no. 4, Jun. 2018. doi:10.1002/rcs.1930
- [21] S.-H. Kim, H.-S. Choi, B. Keum, and H.-J. Chun, "Robotics in gastrointestinal endoscopy," *Applied Sciences*, vol. 11, no. 23, p. 11351, Nov. 2021. doi:10.3390/app112311351
- [22] S. Kim *et al.*, "Colonic endoscopic submucosal dissection using a novel robotic system," *Endoscopy*, Apr. 2022. doi:10.1055/s-0042-1744935

- [23] K.-Y. Ho et al., "Endoscopic submucosal dissection of gastric lesions by using a master and Slave Transluminal Endoscopic Robot (master)," *Gastrointestinal Endoscopy*, vol. 72, no. 3, pp. 593–599, Sep. 2010. doi:10.1016/j.gie.2010.04.009
- [24] K. Kume, "Flexible robotic endoscopy: Current and original devices," *Computer Assisted Surgery*, vol. 21, no. 1, pp. 150–159, Jan. 2016. doi:10.1080/24699322.2016.1242654
- [25] I. Tateya *et al.*, "Flexible next-generation robotic surgical system for transoral endoscopic hypopharyngectomy: A comparative preclinical study," *Head & Neck*, vol. 40, no. 1, pp. 16–23, Nov. 2017, doi: 10.1002/hed.24868.
- [26] B. P. M. Yeung and T. Gourlay, "A technical review of flexible endoscopic multitasking platforms," *International journal of surgery.*, vol. 10, no. 7, pp. 345–354, 2012, doi: 10.1016/j.ijsu.2012.05.009.
- [27] M. Khoshnam and R. V. Patel, "Robotics-Assisted Control of Steerable Ablation Catheters Based on the Analysis of Tendon-Sheath Transmission Mechanisms," *IEEE/ASME Transactions on Mechatronics*, vol. 22, no. 3, pp. 1473–1484, Jun. 2017, doi: <https://doi.org/10.1109/tmech.2017.2688320>.
- [28] S. J. Phee, S. C. Low, P. Dario, and A. Menciassi, "Tendon sheath analysis for estimation of distal end force and elongation for sensorless distal end," *Robotica*, vol. 28, no. 7, pp. 1073–1082, Feb. 2010. doi:10.1017/s026357470999083x
- [29] L. Chen, X. Wang, and W. L. Xu, "Inverse Transmission Model and Compensation Control of a Single-Tendon–Sheath Actuator," *IEEE transactions on industrial electronics : a publication of the IEEE Industrial Electronics Society.*, vol. 61, no. 3, pp. 1424–1433, 2014, doi: 10.1109/TIE.2013.2258300.
- [30] J. Li, J. Lam, M. Liu, and Z. Wang, "Compliant Control and Compensation for A Compact Cable-Driven Robotic Manipulator," *IEEE robotics & automation letters.*, vol. 5, no. 4, pp. 5417–5424, 2020, doi: 10.1109/LRA.2020.3007382.
- [31] G. S. Sawicki and D. P. Ferris, "Mechanics and energetics of level walking with powered ankle exoskeletons," *Journal of experimental biology.*, vol. 211, no. 9, pp. 1402–1413, 2008, doi: 10.1242/jeb.009241.
- [32] B. Jones and I. Walker, "Kinematics for multisection continuum robots," *IEEE transactions on robotics : a publication of the IEEE Robotics and Automation Society.*, vol. 22, no. 1, pp. 43–55, 2006, doi: 10.1109/TRO.2005.861458.
- [33] C. Canudas de Wit, H. Olsson, K. Astrom, and P. Lischinsky, "A new model for control of systems with friction," *IEEE transactions on automatic control.*, vol. 40, no. 3, pp. 419–425, 1995, doi: 10.1109/9.376053.
- [34] P. Puangmali, K. Althoefer, L. D. Seneviratne, D. Murphy, and P. Dasgupta, "State-of-the-Art in Force and Tactile Sensing for Minimally Invasive Surgery," *IEEE sensors journal.*, vol. 8, no. 4, pp. 371–381, 2008, doi: 10.1109/JSEN.2008.917481

- [35] M. Tavakoli, R. V. Patel, and M. Moallem, "A force reflective master-slave system for minimally invasive surgery," vol. 3, pp. 3077–3082, Mar. 2004, doi: 10.1109/iros.2003.1249629.
- [36] C. Riviere and P. Wei Tech Ang, "Toward active tremor canceling in handheld microsurgical instruments," *IEEE transactions on robotics and automation : a publication of the IEEE Robotics and Automation Society.*, vol. 19, no. 5, pp. 793–800, 2003, doi: 10.1109/TRA.2003.817506.
- [37] R. J. Webster and B. A. Jones, "Design and kinematic modeling of Constant Curvature Continuum Robots: A Review," *The International Journal of Robotics Research*, vol. 29, no. 13, pp. 1661–1683, Jun. 2010. doi:10.1177/0278364910368147
- [38] J.-J. Lee and L.-W. Tsai, "The structural synthesis of tendon-driven manipulators having a pseudotriangular structure matrix," *The International Journal of Robotics Research*, vol. 10, no. 3, pp. 255–262, Jun. 1991. doi:10.1177/027836499101000306
- [39] Z. Wang, Z. Sun, and S. J. Phee, "Haptic feedback and control of a flexible surgical endoscopic robot," *Computer Methods and Programs in Biomedicine*, vol. 112, no. 2, pp. 260–271, Nov. 2013. doi:10.1016/j.cmpb.2013.01.018
- [40] A. M. Okamura, "Haptic feedback in robot-assisted minimally invasive surgery," *Current opinion in urology.*, vol. 19, no. 1, pp. 102–107, 2009, doi: 10.1097/MOU.0b013e32831a478c.
- [41] W. Lai et al., "Distal end force sensing with optical fiber Bragg gratings for tendon-sheath mechanisms in flexible endoscopic robots," 2018 IEEE International Conference on Robotics and Automation (ICRA), May 2018. doi:10.1109/icra.2018.8461090
- [42] A. Abiri *et al.*, "Multi-Modal Haptic Feedback for Grip Force Reduction in Robotic Surgery," *Scientific reports.*, vol. 9, no. 1, 2019, doi: 10.1038/s41598-019-40821-1.
- [43] M. Kaneko, M. Wada, H. Maekawa, and K. Tanie, "A new consideration on tendon-tension control system of robot hands," *Proceedings. 1991 IEEE International Conference on Robotics and Automation*, 1991. doi:10.1109/robot.1991.131727
- [44] M. Kaneko, T. Yamashita, and Kazuo Tanie, "Basic considerations on transmission characteristics for tendon drive robots," Jan. 1991, doi: https://doi.org/10.1109/icar.1991.240572.
- [45] V. Agrawal, W. J. Peine, and Bin Yao, "Modeling of a closed loop cable-conduit transmission system," 2008 IEEE International Conference on Robotics and Automation, May 2008. doi:10.1109/robot.2008.4543731
- [46] Y. Kassahun et al., "Erratum to: Surgical Robotics Beyond Enhanced Dexterity Instrumentation: A survey of machine learning techniques and their role in intelligent and autonomous surgical actions," *International Journal of Computer Assisted Radiology and Surgery*, vol. 11, no. 5, pp. 847–847, Jan. 2016. doi:10.1007/s11548-015-1340-9

- [47] T. Li, F. Chen, and Y. Su, "In Situ Calibration of a Six-Axis FBG Force/Moment Sensor for Surgical Robot," *Lecture notes in computer science*, pp. 59–68, Jan. 2022, doi: 10.1007/978-3-031-13835-5_6.
- [48] N. Kai Xu, "Actuation compensation for flexible surgical snake-like robots with redundant remote actuation," in *2006 IEEE International Conference on Robotics and Automation*, [Place of publication not identified]: I E E E, 2006, pp. 33–4154. doi: 10.1109/ROBOT.2006.1642340.
- [49] J. Guo *et al.*, "A novel robotic catheter system with force and visual feedback for vascular interventional surgery," *International Journal of Mechatronics and Automation*, vol. 2, no. 1, p. 15, 2012, doi: 10.1504/ijma.2012.046583.
- [50] K. Wang *et al.*, "Design and Performance Evaluation of Real-time Endovascular Interventional Surgical Robotic System with High Accuracy," *The International Journal of Medical Robotics and Computer Assisted Surgery*, vol. 14, no. 5, p. e1915, May 2018, doi: <https://doi.org/10.1002/rcs.1915>.
- [51] J. Hong, D. Hong, and B. G. Kim, "Modeling backlash-like hysteresis of tendon sheath mechanism-pair," *Journal of Mechanisms and Robotics*, vol. 12, no. 4, Mar. 2020. doi:10.1115/1.4046034
- [52] M. Tavakoli, A. Aziminejad, R. Patel, and M. Moallem, "High-Fidelity Bilateral Teleoperation Systems and the Effect of Multimodal Haptics," *IEEE transactions on systems, man, and cybernetics. a publication of the IEEE Systems, Man, and Cybernetics Society.*, vol. 37, no. 6, pp. 1512–1528, 2007, doi: 10.1109/TSMCB.2007.903700.
- [53] I. D. Walker, "Continuous Backbone 'Continuum' Robot Manipulators," *ISRN Robotics*, vol. 2013, pp. 1–19, Jul. 2013, doi: 10.5402/2013/726506.
- [54] H. Kawasaki, T. Komatsu, and K. Uchiyama, "Dexterous anthropomorphic robot hand with distributed tactile sensor: Gifu hand II," *IEEE/ASME transactions on mechatronics : a joint publication of the IEEE Industrial Electronics Society and the ASME Dynamic Systems and Control Division.*, vol. 7, no. 3, pp. 296–303, 2002, doi: 10.1109/TMECH.2002.802720.
- [55] U. Kim, D.-H. Lee, W. J. Yoon, B. Hannaford, and H. R. Choi, "Force Sensor Integrated Surgical Forceps for Minimally Invasive Robotic Surgery," *IEEE transactions on robotics : a publication of the IEEE Robotics and Automation Society.*, vol. 31, no. 5, pp. 1214–1224, 2015, doi: 10.1109/TRO.2015.2473515.
- [56] A. Bicchi and V. Kumar, "Robotic grasping and contact: a review," in *Robotics and Automation, 2000 IEEE International Conference*, [Place of publication not identified]: I E E E, 2000, pp. 686–353. doi: 10.1109/ROBOT.2000.844081.
- [57] B. Siciliano and O. Khatib, *Springer handbook of robotics*. Berlin: Springer, 2016.
- [58] H. Asada and J.-J. E. Slotine, *Robot analysis and control*. New York, N.Y.: J. Wiley, 1986.

- [59] C. Y. Kim, M. C. Lee, R. B. Wicker, and S.-M. Yoon, "Dynamic modeling of coupled tendon-driven system for surgical robot instrument," *International Journal of Precision Engineering and Manufacturing*, vol. 15, no. 10, pp. 2077–2084, Oct. 2014, doi: 10.1007/s12541-014-0566-8.
- [60] P. F. Hokayem and M. W. Spong, "Bilateral teleoperation: An historical survey," *Automatica*, vol. 42, no. 12, pp. 2035–2057, Dec. 2006, doi: 10.1016/j.automatica.2006.06.027.
- [61] Robotis, "MX-106R, MX-106T (Protocol 2.0)," e-Manual, <https://emanual.robotis.com/docs/en/dxl/mx/mx-106-2/> (accessed Aug. 2, 2024).